

Roto-Translation Equivariant Super-Resolution of Two-Dimensional Flows Using Convolutional Neural Networks

Yuki Yasuda^{a)}

(*Electronic mail: yasuda.y.aa@m.titech.ac.jp)

(Dated: 18 May 2022)

Convolutional neural networks (CNNs) often apparently process vectors as quantities that have no direction such as colors in images. This study investigates the effect of considering vectors as geometric objects in terms of super-resolution of velocity on two-dimensional fluids. Vector is distinguished from scalar by the transformation law associated with a change in basis, which can be incorporated as prior knowledge using the equivariant deep learning. The existing CNNs are converted into equivariant ones by rendering each layer equivariant with respect to rotation and translation. The training data in the high- and low-resolution are generated with the fluid simulation and downsampling, respectively. The inference of the equivariant CNNs is not highly accurate or robust, compared with the conventional CNNs. The conventional CNNs can learn the equivariance and recognize vector directions, adapting to the symmetry of data. In contrast, the equivariant CNNs do not have this flexibility and their inference can be sensitive to the method of data generation. The main advantage of equivariant CNNs is the trainability with a smaller size of data due to the reduction in the parameters. The conclusion of this paper is negative toward the use of equivariant CNNs in super-resolution tasks, which is in contrast to previous studies that apply equivariant neural networks to other fluid mechanics tasks. The effect of incorporating the geometric equivariance in neural networks has yet to be sufficiently explored. It will be necessary to conduct super-resolution with more general configurations such as flows on irregular grids.

I. INTRODUCTION

In recent years, neural networks (NNs) have been actively applied to the field of fluid mechanics.^{1–4} The physical validity of inference of NNs is important both in theory and application. One method to enhance the validity involves explicitly incorporating physics laws such as the Navier-Stokes equations into NNs, which is referred to as the physics-informed neural network.⁵ This method has been extensively studied recently.^{6,7}

Vector is an essential quantity in physics. In applications of NNs to fluids, however, vectors are often apparently processed as direct products of scalars such as colors in images, and convolutional neural networks (CNNs) are employed as in computer vision. Intuitively, vector has direction, whereas scalar does not. This distinction can be mathematically formulated by the covariance in geometry.^{8,9} The covariance describes the manner in which the components of a tensor (e.g., scalar and vector) change under a change of basis associated with a certain coordinate transformation. These transformation laws distinguish the rank of tensors and can be regarded as a part of the definition of scalars and vectors.¹⁰ In other words, by changing the direction of observation through a coordinate transformation, it is possible to determine whether a numerical array is a vector having a direction or a combination of scalars having no direction.

The covariance ensures that scalar and vector themselves are geometrically invariant objects, although their components may be changed under coordinate transformations. Consequently, this leads to the invariance of physics laws de-

scribed with scalars and vectors; that is, the forms of physics equations are independent of coordinate systems. On incorporation of both covariance and physics laws into NNs as prior knowledge, the NNs can be applied to data on any coordinate system without compromising on the accuracy and physical validity. Such NNs incorporating geometric symmetries have been applied to various systems^{11,12} including fluid systems.^{13–18}

Super-resolution (SR) refers to methods of estimating high-resolution images from those with low-resolution. SR is studied in computer vision as an application of NNs.^{19–23} The success of such NNs has resulted in an increased number of studies that focus on the fluid-related SR: idealized turbulent flows in two^{24–30} and three dimensions,^{28,29,31–33} Rayleigh–Bénard convection,³⁴ smoke motions in turbulent flows,^{35–37} flows in blood vessels,^{38–40} sea surface temperature,^{26,41} and atmospheric fields.^{42–49} Physics laws such as the continuity equation can be considered as prior knowledge, rendering super-resolved flows more accurate and physically valid.^{27,32,40} However, studies investigating SR models in terms of geometry are scarce, and the invariance of physics equations has yet to be fully exploited.

The covariance in SR can be satisfied by imposing the equivariance on NNs. The equivariance of a function is defined as the property that the output is transformed according to a transformation of the input. For instance, if an SR model is equivariant, rotating the input results in the output being rotated in the same manner (Fig. 1). Therefore, if the input is a vector field, the output satisfies the same transformation law, assuring that the output is a geometric vector. Importantly, when an SR model is equivariant to rotation, the model is applicable to data in any orientation. This fact suggests that the equivariance needs to reflect the rotational symmetry of fluid systems. The terms of covariance, equivariance, and symmetry are clarified in the later section.

^{a)}Global Scientific Information and Computing Center, Tokyo Institute of Technology,
2-12-1 Ookayama, Meguro-ku, Tokyo 1528550, Japan

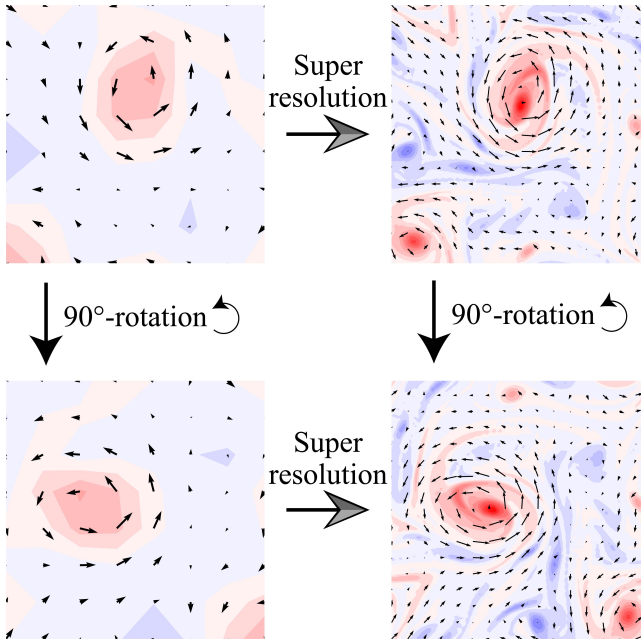


FIG. 1. Schematic for the equivariance of super-resolution. If a super-resolution model is equivariant to rotation, the rotation is commutative with the super-resolution. The colors represent a scalar field and the arrows represent a vector field.

The success of conventional CNNs can be attributed to the translation equivariance. For instance, when an object in an image is translated, the output feature is translated in the same manner. In other words, the feature extraction by the conventional CNN is independent of object positions. CNNs with other types of equivariance (e.g., rotation) have been studied.^{50–57} These CNNs can be understood within unified frameworks^{58–60} on the equivariant CNNs that are based on the group theory^{61,62} and differential geometry.^{8,9} The theories and techniques on the equivariant CNN have been developed not only for two-dimensional images, but also for graph data⁶³ and three-dimensional volumetric⁶⁴ and point cloud data.⁶⁵ Those studies can be considered a part of the geometric deep learning.^{11,12}

In computer vision, the equivariance has sometimes been utilized in SR. The equivariance can be incorporated into loss functions^{66,67} or discriminators of generative adversarial networks (GANs).⁶⁸ Both methods facilitate that an image generator acquires the equivariance from training data. Few studies directly impose the equivariance on image generators of SR. Xie et al.⁶⁹ develops an SR model with a self-attention module. In their module, the point-wise convolution is utilized to construct key, query, and value, resulting in the equivariance to any pixel permutation. Although their module is equivariant to various transformations, it cannot be applied to vector fields.

In fluid mechanics, several studies have employed equivariant NNs: the modeling of Reynolds stress tensors,^{17,18,70} the surrogate modeling of the governing equations,^{14,15} the flow estimation over several particles,¹⁶ and the estimation of higher-rank tensors of fluids.¹³ Those studies incorporate the

physics symmetries using the equivariant NNs and report that the equivariance enhances the accuracy or robustness of inference. To the best of the author's knowledge, however, the effect of including symmetries has not been examined in terms of the fluid SR.

This paper aims to clarify whether the equivariance improves the accuracy and robustness of super-resolution of velocity fields. If a deterioration in accuracy is observed, the cause is investigated. To highlight the essence, simple two-dimensional velocity fields are super-resolved. The equivariance to rotation and translation are considered, both of which are fundamental in physics. The two existing CNNs^{25,32} for the fluid SR are converted into equivariant ones, and the inference is compared between the original and equivariant CNNs. The following things are demonstrated:

- The incorporation of the rotational symmetry does not necessarily enhance the accuracy and robustness of SR. When the deterioration occurs, a cause is attributed to the symmetry breaking through the data generation, which can easily arise via a slight change in the scale factor of SR.
- When the data preserve the rotational symmetry, the accuracy of the equivariant CNNs is comparable to that of the original ones. Further, the equivariant CNNs are trainable with a smaller size of the data owing to the reduction in the learnable parameters.
- The original CNNs learn the equivariance from the data even without data augmentation, indicating that these trained CNNs recognize vector directions. This result explains why there is no significant difference in accuracy between the original and equivariant CNNs.
- When the data do not exhibit the rotational symmetry, the accuracy of the equivariant CNNs is lower than that of the original ones. In this case, the inference depends on the orientation of the data, and vector should be treated as a quantity having no direction by using the original, non-equivariant CNNs.

The remaining paper is organized as follows. Section II clarifies the terms such as equivariance and then reviews a theory of equivariant CNNs.⁶⁰ Section III describes all CNNs used in this study. Section IV gives the methods of training and evaluating the CNNs. Section V analyzes the results with and without the rotational symmetry in the data. The conclusions are presented in Section VI. The source code of this study is available on the GitHub repository.⁷¹

II. THEORETICAL BACKGROUND ON EQUIVARIANT CNNS

This section briefly explains the theoretical background on equivariant CNNs. The mathematical terms are defined in Section II A. A theory of equivariant CNNs⁶⁰ is reviewed in Sections II B - II D.

The notations are clarified first. This paper considers the two-dimensional Euclidean space using the Cartesian coordinate system: $\mathbf{x} = (x, y)^T \in \mathbb{R}^2$. A combination of translation and rotation is represented by the special Euclidean group $SE(2)$ or a subgroup of $SE(2)$. Scalar (i.e., tensor of rank 0) and vector (i.e., tensor of rank 1) are mainly considered. Contravariant and covariant vectors are identified because of the orthonormal basis on the Cartesian coordinates. There are two types of transformations in the tensor analysis: active and passive transforms. In the former, scalar and vector themselves are transformed, whereas the coordinates remain fixed. In contrast, in case of the latter, the opposite treatment is adopted. The active transform is employed following the previous studies on equivariant CNNs.^{59,60} When using the passive transform, it is stated clearly.

A. Covariance, equivariance, and symmetry

The covariance, equivariance, and symmetry are clarified for this study. Mathematical details are found in Refs. 8, 9, 11, and 60.

The translation and rotation are defined using a position vector $\mathbf{x} = (x, y)^T$:

$$\tau_t \mathbf{x} = \mathbf{x} + \mathbf{t}, \quad (1a)$$

$$\rho_\theta \mathbf{x} = \begin{pmatrix} \cos \theta & -\sin \theta \\ \sin \theta & \cos \theta \end{pmatrix} \begin{pmatrix} x \\ y \end{pmatrix}, \quad (1b)$$

where \mathbf{t} is a translation vector and θ is a rotation angle. The inverse transforms are represented as $\tau_t^{-1} \mathbf{x} = \tau_{-t} \mathbf{x}$ and $\rho_\theta^{-1} \mathbf{x} = \rho_{-\theta} \mathbf{x}$. A combination of translation and rotation is formulated as follows, which is a member of $SE(2)$:

$$\tau_t \rho_\theta \mathbf{x} = (\rho_\theta \mathbf{x}) + \mathbf{t}. \quad (2)$$

If there is no confusion, the subscripts of t and θ are omitted.

The covariance provides the transformation laws for a scalar $\omega(\mathbf{x})$ and a vector field $\mathbf{v}(\mathbf{x})$ under rotation and translation:

$$g_{\text{scalar}} : \omega(\mathbf{x}) \mapsto \omega((\tau \rho)^{-1} \mathbf{x}) \quad [= \omega(\rho^{-1}(\mathbf{x} - \mathbf{t}))], \quad (3a)$$

$$g_{\text{vector}} : \mathbf{v}(\mathbf{x}) \mapsto \rho \mathbf{v}((\tau \rho)^{-1} \mathbf{x}) \quad [= \rho \mathbf{v}(\rho^{-1}(\mathbf{x} - \mathbf{t}))], \quad (3b)$$

$$g : F(\mathbf{x}) \mapsto \pi(\rho) F((\tau \rho)^{-1} \mathbf{x}) \quad [= \pi(\rho) F(\rho^{-1}(\mathbf{x} - \mathbf{t}))], \quad (3c)$$

Only the referred position is changed for a scalar as in (3a), whereas in case of a vector, both the referred position and components are changed as in (3b). The change in the vector components describes the change in its direction. When scalars or vectors are piled onto a numerical array, each is independently transformed according to (3a) or (3b). Both scalars and vectors satisfy the linearity. The transformation law, namely the covariance, distinguishes between scalar and vector. The last equation (3c) can be used to any combination of any tensor fields, where the representation of $\pi(\rho)$ depends on F : $\pi(\rho) = 1$ for a scalar; $\pi(\rho) = \rho$ for a vector; $\pi(\rho)$ is a block diagonal matrix consisting of ρ when F is a stack of vectors.

The transformation laws can be mathematically derived from the definition of tensors. In physics, the converse treatment is sometimes adopted:¹⁰ if a quantity satisfies one of the transformation laws, it is identified as a tensor and called covariant. Most governing equations in physics (e.g., Navier-Stokes and Maxwell equations) satisfy the covariance.⁷² In this case, both sides of an equation obey the same transformation, and the form of the entire equation is independent of rotation and translation. In passive transforms, the covariance assures that a geometric quantity such as vector is itself invariant, even if its components are changed due to a change of basis. This fact leads to the invariance of the form of physics equations.

The equivariance is defined as the commutativity of a function f with transformations g . Consider a function $f : F_{\text{in}} \mapsto F_{\text{out}}$, where F_{in} is a scalar or vector field and for simplicity F_{out} is assumed to be a field of the same type as F_{in} . The function f is equivariant if it satisfies

$$(f \circ g)(F_{\text{in}}) = (g \circ f)(F_{\text{in}}) = g(F_{\text{out}}). \quad (4)$$

For instance, when g represents a rotation, the rotated input $g(F_{\text{in}})$ yields $f(g(F_{\text{in}}))$, which is equal to the rotated output $g(F_{\text{out}})$ (Fig. 1). The transformation g composes a group such as $SE(2)$, and Eq. (4) must hold for all elements of the group. Note that the invariance is regarded as a special case of the equivariance: $(f \circ g)(F_{\text{in}}) = F_{\text{out}}$, where F_{out} is independent of g . Equation (4) indicates that if f is equivariant to appropriate transformations, F_{in} and F_{out} are covariant, i.e., they follow the same transformation.

The symmetry in theoretical physics is described with Lagrangian.⁷² If the form of a Lagrangian is invariant to certain transformations, the system has the symmetry. In deep learning, the term of symmetry is used in a broader sense:¹¹ if a certain property of a system or object is unchanged under a transformation, the system or object is said to have the symmetry. In this paper, if an NN is equivariant to rotation and translation, it is called symmetric. This definition may be natural because the equivariance leads to the covariance and the covariance assures the geometric invariance of tensors as discussed above. For fluid systems, the term of symmetry is used in the conventional sense in physics. If a fluid system has rotational symmetry, the form of the governing equations is invariant and a rotated flow is a solution.

B. Linear constraint on equivariant kernels of convolution

In the remainder of this section, a theory on the equivariant CNNs^{59,60} is briefly reviewed. The aim is to explain a trade-off between the expressive power and equivariance, but not present the details of the theory. This trade-off has rarely been emphasized in the previous studies.^{14,18,59,60} This subsection discusses a linear constraint that is satisfied by equivariant kernels. The following two subsections give examples to clarify the meaning of the constraint and trade-off.

The convolution is defined by

$$F_{\text{out}}(\mathbf{y}) = \kappa * F_{\text{in}} = \int \kappa(\mathbf{y} - \mathbf{x}) F_{\text{in}}(\mathbf{x}) \, d\mathbf{x}, \quad (5)$$

where $*$ stands for the convolution, the input F_{in} and output F_{out} are tensors generally having different ranks, κ is a kernel, and the integral is performed over the continuous Euclidean plane without boundary. The multiplication between κ and F_{in} is generally a matrix operation. Consider that F_{in} and F_{out} are transformed by a combination of rotation and translation as in (3c):

$$g_{\text{in}} : F_{\text{in}}(\mathbf{x}) \mapsto \pi_{\text{in}}(\rho) F_{\text{in}}(\rho^{-1}(\mathbf{x} - \mathbf{t})) , \quad (6a)$$

$$g_{\text{out}} : F_{\text{out}}(\mathbf{x}) \mapsto \pi_{\text{out}}(\rho) F_{\text{out}}(\rho^{-1}(\mathbf{x} - \mathbf{t})) . \quad (6b)$$

If the kernel κ satisfies the following linear constraint, the convolution (5) is equivariant.^{59,60,64}

$$\pi_{\text{out}}(\rho) \kappa(\mathbf{x}) = \kappa(\rho \mathbf{x}) \pi_{\text{in}}(\rho) . \quad (7)$$

Following Ref. 60, the equivariance of the convolution is confirmed:

$$\begin{aligned} \kappa * g_{\text{in}}(F_{\text{in}}) &= \int \kappa(\mathbf{y} - \mathbf{x}) \pi_{\text{in}}(\rho) F_{\text{in}}(\underbrace{\rho^{-1}(\mathbf{x} - \mathbf{t})}_{\mathbf{x}'}) d\mathbf{x} , \\ &= \int \kappa(\mathbf{y} - \mathbf{t} - \rho \mathbf{x}') \pi_{\text{in}}(\rho) F_{\text{in}}(\mathbf{x}') d\mathbf{x}' , \\ &= \int \underbrace{\kappa(\rho(\rho^{-1}(\mathbf{y} - \mathbf{t}) - \mathbf{x}'))}_{\pi_{\text{out}}(\rho) \kappa(\rho^{-1}(\mathbf{y} - \mathbf{t}) - \mathbf{x}')} \pi_{\text{in}}(\rho) F_{\text{in}}(\mathbf{x}') d\mathbf{x}' , \\ &= \pi_{\text{out}}(\rho) F_{\text{out}}(\rho^{-1}(\mathbf{y} - \mathbf{t})) , \\ &= g_{\text{out}}(F_{\text{out}}) , \end{aligned} \quad (8)$$

where the fact that the Jacobian is unity under rotation is exploited. Equation (8) means that the output F_{out} is rotated according to a rotation of the input F_{in} , which corresponds to the definition of the equivariance (4). In application, a convolution kernel is given by a linear combination of the solution of (7).

A few important mathematical results in Ref. 64 are mentioned here. The constraint (7) is not only sufficient but also necessary for the equivariance of convolution. Moreover, a linear map is equivariant if and only if the map is an equivariant convolution. In the derivation of (7), the two-dimensionality is not exploited; hence, the same constraint can be derived in the three-dimensional Euclidean space.

C. Example1: trivial representation with spatially varying kernel

The linear constraint (7) is interpreted using two simple examples. First, the effect of changes in position is discussed. Consider that the input and output are scalars. Scalar has the trivial representation,^{61,62} i.e., all $\pi(\rho)$ such as in (6) become unity. Consequently, the constraint (7) becomes

$$\kappa(\mathbf{x}) = \kappa(\rho \mathbf{x}) , \quad (9)$$

where $\kappa(\mathbf{x})$ is a real number depending on \mathbf{x} and $\kappa(\mathbf{x})$ acts on a scalar field.

The rotation in multiples of 120° is considered as an example. A pattern having the wavenumber-3 structure such

as $\cos(3\theta)$ is a solution to (9). Such a kernel is invariant to the rotation, implying that the output is rotated according to a rotation applied to the input. The radial structure is not determined by (9); usually, a certain form such as Gaussian is assumed and its amplitude is optimized by training.^{53,60}

There is a trade-off between the expressive power and equivariance. For the conventional convolution, a kernel can learn an azimuthal pattern from data, whereas it is not necessarily equivariant. This is in contrast to the equivariant kernels: the azimuthal pattern is determined by the constraint (9), which guarantees the equivariance.

D. Example2: regular representation with spatially uniform kernel

The effect of $\pi(\rho)$ in (7) is discussed next. Consider that the kernel is spatially uniform and the input and output are described with the same representation. Equation (7) is simplified as follows:

$$\pi(\rho) \kappa = \kappa \pi(\rho) , \quad (10)$$

where the subscripts of “out” and “in” are omitted and the matrix κ does not depend on position.

The rotation in multiples of 120° is considered again. The regular representation^{61,62} is employed here, where the rotation is formulated as a permutation. Figure 2 is a schematic describing the action of the 120° rotation on a set of features. Each feature can be identified as a vertex of an equilateral triangle. The rotation is regarded as the permutation of these vertices.

Mathematically, the set of features in Fig. 2, namely $(a, b, c)^T$, is not a geometric vector; rather, it is regarded as a linearly transformed vector. The feature set $(a, b, c)^T$ can be complex numbers, which also implies that it is not a geometric vector. Ref. 60 discusses the mathematical details such as the difference between the real and complex representations.

In the regular representation, all rotations in multiples of 120° are described with the following three matrices and combinations thereof:

$$\pi(\theta = 0) = \begin{pmatrix} 1 & 0 & 0 \\ 0 & 1 & 0 \\ 0 & 0 & 1 \end{pmatrix} , \quad (11a)$$

$$\pi(\theta = 120^\circ) = \begin{pmatrix} 0 & 0 & 1 \\ 1 & 0 & 0 \\ 0 & 1 & 0 \end{pmatrix} , \quad (11b)$$

$$\pi(\theta = 240^\circ) = \begin{pmatrix} 0 & 1 & 0 \\ 0 & 0 & 1 \\ 1 & 0 & 0 \end{pmatrix} , \quad (11c)$$

where the argument of π is denoted by the rotation angle θ instead of the rotation matrix ρ .

The constraint (10) must hold for all three matrices in (11). The solution is

$$\begin{pmatrix} \kappa_1 & \kappa_2 & \kappa_3 \\ \kappa_3 & \kappa_1 & \kappa_2 \\ \kappa_2 & \kappa_3 & \kappa_1 \end{pmatrix} , \quad (12)$$

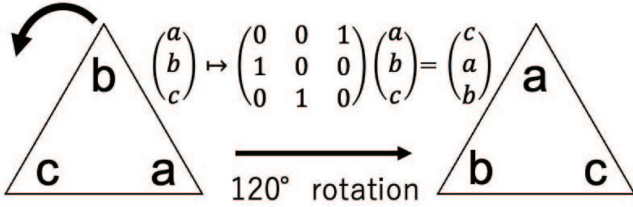


FIG. 2. Schematic describing the action of the 120° rotation on a set of features $(a, b, c)^T$ with the regular representation. The matrix of $\pi(\theta = 120^\circ)$ in (11b) is used in the figure.

where κ_1 , κ_2 , and κ_3 are learnable parameters that are determined by training. The kernel (12) has the symmetric structure, which leads to the commutative property of the kernel multiplication with the permutation representing the rotation. The equivariant kernel (12) has only 3 learnable parameters, although it is a 3×3 matrix. In the conventional convolution, when a kernel is 3×3 , i.e., 3 channels are transformed into 3 channels, all 9 parameters are learnable. This is another example of trade-off between the expressive power and equivariance. A convolution kernel that satisfies the constraint (7) is equivariant, while its parameters are not free in the channel dimension as well as in the spatial dimension.

III. CNNS USED IN THIS RESEARCH

Many network architectures for the fluid SR have been proposed (Section I). To fully exploit those results, the effect of converting the proposed networks to equivariant ones must be examined. Two CNNs were employed here: hybrid downsampled skip-connection/multi-scale (DSC/MS) model by Fukami et al.²⁵ and residual in residual dense network (RRDN) by Bode et al.³² Equivariant CNNs were obtained from the DSC/MS and RRDN by rendering each layer equivariant. The use of the two kinds of networks can confirm that the results in this paper are not strongly dependent on the network structure. Section III A reviews the DSC/MS and RRDN. Section III B discusses the conversion to the equivariant networks.

A. Two CNNs for super-resolution of fluids

The hybrid DSC/MS model (hereafter, DSC/MS) was proposed in pioneering work on the fluid SR by Fukami et al.²⁵ They combined their model of downsampled skip connection (DSC) with the multi-scale (MS) model.⁷³ Figure 3 shows the network architecture of the DSC/MS used here. Multi-scale signals in a fluid field can be captured by the downsampling and skip connections. The DSC/MS can super-resolve both velocity and vorticity fields in two dimensions.²⁵ In the subsequent studies, the DSC/MS has been applied to the three-dimensional velocity;^{28,29} the spatio-temporal SR has been performed by the successive use of DSC/MS in space and time;²⁹ a deeper version of the DSC/MS has been proposed.³⁰

Although the DSC/MS was proposed relatively early, it is still among the most important CNNs in the fluid SR.

The RRDN utilizes residual in residual dense block (RRDB),^{21,74} which extracts multi-scale structures in a fluid field with dense skip connections. Figure 4 shows the network architecture of the RRDN used here. Bode et al.³² proposed the RRDN as the generator of their physics-informed GAN and applied the GAN to the three-dimensional velocity. A similar network to the RRDN has been employed for the SR of two-dimensional passive scalars.²⁷ The RRDB, which is the core module of the RRDN, is utilized for the SR in fluid mechanics^{27,32} as well as in computer vision.^{21,74} Thus, an equivariant CNN having RRDBs needs to be investigated.

The input of the DSC/MS or RRDN is a snapshot of either velocity or vorticity and the output is the super-resolved field at the instantaneous time; that is, the single-image super-resolution is performed in this paper.

B. Construction of equivariant CNNs

The DSC/MS and RRDN are converted into equivariant ones by replacing all layers with the equivariant counterparts. Mathematically, if each layer is equivariant, the entire network is equivariant.^{11,60} The replacement of convolution layers is discussed first, and then the implementation of the other layers is described.

The discretization of rotation and the group representation are explained before discussing the configuration of convolution. In practice, scalar and vector fields need to be discretized in space, and the rotation acting on them is discretized as well. This paper focuses on the discrete rotation in multiples of 90° or 180° . These rotations do not require spatial interpolation or extrapolation. Furthermore, these rotations reflect the rotational symmetries of the fluid systems described in the next section. The rotations in multiples of 90° ($= 360^\circ/4$) and 180° ($= 360^\circ/2$) are mathematically described by the cyclic groups of order 4 and 2, i.e., C_4 and C_2 , respectively. CNNs equivariant to these rotations are referred to as C_4 - and C_2 -equivariant.

An important hyperparameter in the equivariant convolution is the group representation.⁶⁰ The representation of rotation, namely $\pi(\rho)$ in (3c), depends on the basis of the linear space on which the rotation acts. This study adopted the regular representation of C_N in all hidden layers. In this representation, rotation is formulated as a permutation. An example of the regular representation of C_3 has been discussed in Section II D. There are three reasons for adopting the regular representation. First, this comprises all irreducible representations, i.e., all minimal representations.^{61,62} Second, the CNNs using the regular representation have exhibited high accuracy in image classification.^{50–52,60} Third, each channel can be transformed nonlinearly and independently when the regular representation is used.^{50,60} In contrast, when another representation is employed, each channel may not be transformed independently by a nonlinear function such as ReLU. A function such as Norm-ReLU⁶⁰ is necessary, as it acts on the vector norm and preserves the vector direction. A limitation such as in Norm-ReLU may reduce the expressive power of CNNs and

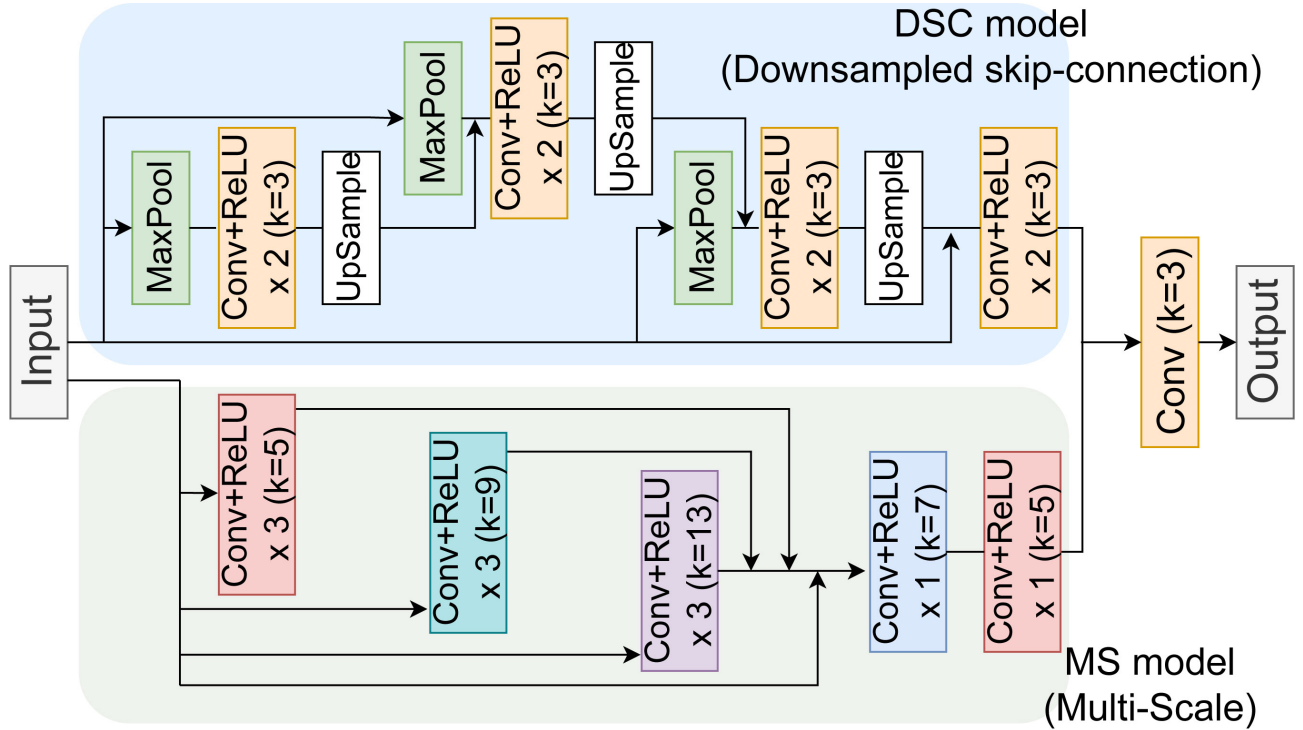


FIG. 3. Network architecture of the hybrid DSC/MS model (Downsampled Skip-Connection and Multi-Scale). The architecture follows the CNN proposed by Fukami et al.²⁵ All convolutions are two-dimensional. The symbol k denotes the spatial size of kernel. The linear interpolation is used in upsampling.

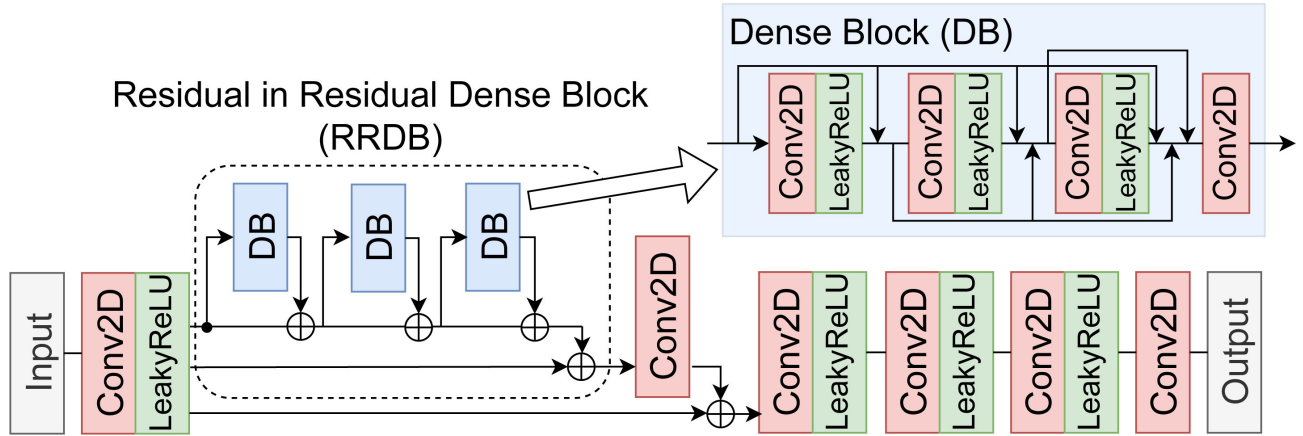


FIG. 4. Network architecture of the RRDN (Residual in Residual Dense Network). The architecture follows the generator of the GAN proposed by Bode et al.³² All kernels in the convolution layers have the spatial size of 3×3 .

may not be suitable for SR.

Equivariant versions of the DSC/MS and RRDN are referred to as the Eq-DSC/MS and Eq-RRDN, respectively. All convolution layers in the original models are replaced with the equivariant ones, while maintaining the number of channels to make the calculation time nearly the same. For instance, the regular representation of C_4 is composed of the 4 elements. If both input and output of a convolution layer have 64 channels, the C_4 -equivariant convolution employs 16 sets of the regular representation. The other hyperparameters such as kernel size

are the same as in the original convolution layers.

The implementation of the other layers is as follows. A max-pooling layer is replaced with the norm max-pooling^{52,60} when the input is a vector field, whereas it remains unchanged when the input is scalar or described by the regular representation. In all cases, the pooling operation is equivariant.^{50,52,60} The linear or bicubic interpolation is used in resizing data, both of which are equivariant because the weights of interpolation depend only on the absolute difference in x or y coordinates.⁷⁵ The skip connection needs no replacement¹⁴

because it is an addition operation between features having the same type. A channel-wise nonlinear function such as ReLU and leaky ReLU is equivariant because of the regular representation as discussed above.

The representation of the input or output of the entire network is determined as follows. When the input or output is scalar, it is regarded as a feature field with the trivial representation.^{61,62} A vector field is naturally considered as a feature with the irreducible representation of order 1.^{61,62} In both cases, any conversion is not necessary.

IV. METHODOLOGY

This section presents the methods of training and testing the CNNs. The high-resolution (HR) data are generated from the numerical simulations that solve the governing equations (Section IV A). Whereas, the low-resolution (LR) data are obtained by downsampling the HR ones (Section IV B). The supervised training is performed using the pairs of the HR and LR data (Section IV C). The evaluation metrics are defined in Section IV D. The source code of this paper is available on the GitHub repository.⁷¹

A. Fluid dynamics simulations

Two types of experiments were conducted: freely-decaying turbulence on a square flat torus and barotropic instability on a periodic channel. The rotational symmetries of the two fluid systems are different as described below. Thus, the dependence on symmetry can be examined by comparing the results.

The governing equations for all experiments are as follows:

$$\frac{\partial \omega}{\partial t} + u \frac{\partial \omega}{\partial x} + v \frac{\partial \omega}{\partial y} = -v(-\Delta)^{n_v} \omega, \quad (13a)$$

$$(u, v) = \left(-\frac{\partial \psi}{\partial y}, \frac{\partial \psi}{\partial x} \right), \quad (13b)$$

$$\omega = \Delta \psi = \frac{\partial v}{\partial x} - \frac{\partial u}{\partial y}, \quad (13c)$$

where t denotes time, v is a positive real number, and n_v is a positive integer. The velocity components (u, v) are obtained using the stream function ψ in (13b), which is derived by solving the Poisson equation (13c) with the vorticity ω . For the two-dimensional translation and rotation, the vorticity is regarded as a scalar field, whereas the velocity is a vector field. Note that large-scale flows in the ocean and atmosphere are described by similar equations⁷⁶ (i.e., quasi-geostrophic equations); the only difference is that the Poisson equation is three-dimensional and includes the altitude or depth dimension.

The governing equations (13) were numerically solved with the spectral method. A software library, ISPACK⁷⁷ coded with Fortran, was employed to perform spectral calculations. The discrete Fourier transform was used in a periodic direction,

whereas the discrete sine/cosine transform was used in a direction bounded by two walls. In addition, the fourth-order Runge-Kutta method was utilized for the time integration.

The freely-decaying turbulence experiment was conducted following Refs. 25 and 78. Here, $v = 10^{-2}$ and $n_v = 1$ were set, leading the governing equations (13) to the two-dimensional Navier-Stokes equations. The doubly periodic boundary condition was imposed on the flow domain $[0, 2\pi] \times [0, 2\pi]$. This domain, which is a square flat torus, has the rotational symmetry in multiples of 90° . The grid numbers are 128×128 , which determines the truncation wavenumber of 42 for alias-free simulations. The initial condition was given at random with keeping the energy spectrum of $E(k) = a \times k \exp(-k^2/k_0^2)$, where k is the magnitude of wavenumber vector and $k_0 = 26.5$. The initial Reynolds number Re is controlled by the amplitude a : $Re \approx 80.0$ for the training data ($a = 9$) and $Re \approx 93.3$ for the test data ($a = 12$), which were evaluated following Ref. 25. Subsequently, on varying the random initial condition, 1,000 simulations were run for the training and 100 for the test. In each simulation, 10 snapshots were sampled between $1.1 \leq t \leq 2.0$ at intervals of 0.1. Thus, the training and test datasets comprise 10,000 and 1,000 snapshots, respectively. Test results similar to those shown below were obtained when the test data were halved, implying that the 1,000 snapshots are sufficient for estimating generalization errors.

Barotropic instability is a fundamental mechanism to make the fluid evolution complicated.⁷⁶ Here, $v = 10^{-30}$ and $n_v = 8$ were set, resulting in the governing equations (13) forming the two-dimensional Euler equations with the hyper-viscosity. The channel domain is $[0, 2\pi] \times [-\pi/2, \pi/2]$, where the x direction is periodic and the y direction is bounded by the two walls [$\psi = 0$ ($y = \pm\pi/2$)]. This domain exhibits the rotational symmetry in multiples of 180° . The grid size is 128×65 , which determines the truncation wavenumber of 42 for alias-free simulations. The initial condition was given by the superposition of an unstable laminar flow and random perturbations. The laminar flow has the shear region:

$$u = \begin{cases} U & \left(\frac{w}{2} \leq y \leq \frac{\pi}{2} \right), \\ U + 2U \frac{(y - \frac{w}{2})}{w} & \left(-\frac{w}{2} < y < \frac{w}{2} \right), \\ -U & \left(-\frac{\pi}{2} \leq y \leq -\frac{w}{2} \right), \end{cases} \quad (14)$$

where the shear is controlled by the width w and the speed U . The other velocity component v is zero. The speed was set $U = 0.25$ (positive shear) or -0.25 (negative shear). The numbers of experiments of $U = 0.25$ and -0.25 were kept the same. The width was set $w = 0.45$ for the training data and 0.40 for the test data. In the numerical experiments, the velocity profile (14) was made smooth around $y = \pm w/2$ to avoid the initial discontinuity of the vortex field. The initial perturbation has the constant amplitude of 10^{-4} and a random phase. Subsequently, on varying the random phases, 800 and 80 simulations were run for the training and test, respectively. In each simulation, 14 snapshots were sampled between $31 \leq t \leq 70$ at intervals of 3. Thus, the training and test datasets comprise 11,200 and 1,120 snapshots, respectively. Test results similar to those shown below were obtained when

the test data were halved, implying that the 1,120 snapshots are sufficient to estimate generalization errors.

B. Data preparation

The HR snapshots of velocity or vorticity were generated from the fluid simulations in the previous subsection. The LR snapshots were obtained by downsampling the HR ones. Two downsampling algorithms were used: subsampling and local average. The subsampling means the extraction of pixel values at certain intervals. This operation may be regarded as fluid observation such as particle image velocimetry (PIV).^{33,79} The local average can be used to compress HR fluid data and an SR model is then utilized to decompress the data.⁸⁰ The subsampling and local average have often been employed in the studies of the fluid SR.^{24,25,29–31,33,35,43,45–47,49}

The downsampling is processed in four steps. First, a scale factor s is determined. When $s = 2$, for instance, an LR image is twice as coarse as the HR image. Second, an HR snapshot of size $H \times W$ is resized to $H' \times W'$, where H' (W') is the multiple of s closest to H (W). Third, the downsampling algorithm is applied to the resized HR snapshot: in the subsampling, pixel values are extracted at intervals of $s \times s$; in the local average, each non-overlapping area of $s \times s$ is replaced with its mean. Fourth, the obtained snapshot of $H'/s \times W'/s$ is resized to $H \times W$. The bicubic interpolation⁷⁵ is used in all cases of resizing mentioned above. Regarding the velocity, the algorithm is applied to u or v separately, because each component of vectors is added or subtracted independently in the Cartesian coordinates.

The scale factor s is 5, 9, or 13 in Sections V A and V B, whereas it is 4 or 5 in Section V C. The training and evaluation were conducted separately for each s .

C. Training of CNNs

The CNNs were trained with supervised learning. They were implemented with PyTorch⁸¹ 1.8.0 and e2cnn⁶⁰ 0.2.1. The latter is a software library for the equivariant deep learning of two-dimensional data.

An important hyperparameter of equivariant CNNs is the order N of a cyclic group C_N . For instance, when $N = 3$, a CNN is equivariant to the rotation in multiples of $360^\circ/3 = 120^\circ$. Here, $N = 4$ was set in the decaying turbulence and $N = 2$ in the barotropic instability because the square torus possesses the rotational symmetry of 90° and the channel domain is symmetric for the 180° rotation. The effect of changing N is investigated in Appendix A.

The Adam optimizer was used coupled with the loss function of mean squared error. This loss function is invariant to rotation and translation for scalars and vectors. The mini-batch size for the DSC/MS and Eq-DSC/MS was 100, while that for the RRDN and Eq-RRDN was 32. The learning rate was between 1.0×10^{-3} and 1.0×10^{-4} and was basically the same for the DSC/MS and Eq-DSC/MS and for the RRDN

and Eq-RRDN. Each training was finished via early stopping with the patience parameter of 30 epochs, where 30% of the training data was used for the validation.

Data augmentation was not employed because of the following two reasons. First, the data augmentation is not necessary for equivariant CNNs because they take symmetries into account as the prior knowledge.^{58–60} Second, the data augmentation may impose inappropriate symmetries that the original data do not possess (Section V C). Without the data augmentation, the comparison between the equivariant and original CNNs is clarified, and the symmetry inherent in the data becomes distinct.

D. Evaluation metrics of CNNs

The following three metrics are utilized to evaluate the CNNs: norm error ratio, energy spectral error, and equivariance error ratio.

The norm error ratio (NER)²⁵ is defined as follows:

$$NER = \frac{\sum_{\text{space}} \|Y - \hat{Y}\|}{\sum_{\text{space}} \|Y\|}. \quad (15)$$

The summation is taken over the entire space. The symbol $\|\cdot\|$ denotes the Euclidean norm when the inference \hat{Y} and ground truth Y are vectors, whereas it is the absolute value in case of scalars. In the actual evaluation, the NER (15) was averaged over the entire test sample.

The energy spectral error (ESE) was introduced to evaluate the validity of spatial patterns by Wang et al.¹⁴ The ESE is equal to the root-mean-squared error of the logarithm of the energy spectra between the inference and ground truth:

$$ESE = \sqrt{\frac{1}{M} \sum_{\text{samples}, k} [\log E(k) - \log \hat{E}(k)]^2}, \quad (16)$$

where E (\hat{E}) is the energy spectrum of the ground truth (inference), M is the normalization constant for the mean, and the summation is taken over the wavenumber and the entire test sample. The ESE is interpreted as the error of spatial correlations through the convolution theorem.

Wang et al.¹⁴ also introduced the equivariance error, which measures the equivariance of any model and is calculated without referring to the ground truth. The equivariance error ratio (EER) is defined by

$$EER := \frac{\sum_{\text{central region}} \|(f \circ g)(F_{\text{in}}) - (g \circ f)(F_{\text{in}})\|}{\sum_{\text{central region}} \|(g \circ f)(F_{\text{in}})\|}, \quad (17)$$

where f denotes a CNN and g is a rotation or translation (3). The summation is taken over the central 48×48 pixels to avoid the effect of extrapolation such as zero padding. If the model is exactly equivariant, the EER is equal to zero. In the actual evaluation, the EER (17) was averaged over the entire input sample. Only the rotational transformation is considered below because conventional CNNs are equivariant to translation and the usefulness of CNNs has been confirmed by many studies (Section I).

V. RESULTS

This section evaluates the equivariant and original CNNs. Sections V A and V B discuss cases where the data reflect the rotational symmetries of the fluid systems. A case breaking symmetry is examined in Section V C. Only the SR of velocity is presented owing to similar results in the case of vorticity. Appendix B compares the SR of velocity and vorticity.

A. Freely-decaying turbulence experiment

The freely-decaying turbulence evolves in the square flat torus. This fluid system has the rotational symmetry in multiples of 90° ($= 360^\circ/4$); hence, the C_4 -equivariant models (Eq-DSC/MS and Eq-RRDN) are compared with the original CNNs (DSC/MS and RRDN).

Figure 5 shows an example of the vorticity calculated from the super-resolved velocity, where the scale factor $s = 9$. The finite difference operation in deriving the vorticity emphasizes the small-scale structure in the super-resolved flow. Regarding the baseline of bicubic interpolation, the shape of each vortex is ambiguous and the difference from the ground truth is large. All SR models reproduce well the small-scale structure. The flows inferred by the equivariant models are nearly the same as those by the original ones.

Figure 6 compares the NERs (15) and ESEs (16) from the SR of the subsampled or locally averaged velocity. With increasing the scale factor s , the errors increase. The NER and ESE values of the Eq-DSC/MS and Eq-RRDN are comparable to or slightly smaller than those of the DSC/MS and RRDN, respectively. The previous studies^{13–18} report that the inference of NNs becomes more accurate when the equivariance is imposed as prior knowledge. In our result (Fig. 6), however, the improvement in accuracy is not quite clear compared with the conventional CNNs.

Table I compares the numbers of the trainable parameters in all SR models. The RRDN and Eq-RRDN have one order of magnitude more parameters than the DSC/MS and Eq-DSC/MS, respectively. This fact may explain that the RRDN and Eq-RRDN tend to show lower errors in Fig. 6. The number of parameters is generally smaller in equivariant models than in non-equivariant ones owing to the constraint of the equivariance (Section II B). The C_4 -equivariant models have fewer parameters than the C_2 -equivariant ones because the group of C_4 contains C_2 and the constraint on the C_4 -equivariance is stricter. Note that the C_2 -equivariant models are used in the next subsection. The reduction in parameters implies that the expressive power of the equivariant SR models is lower in principle. However, the Eq-DSC/MS and Eq-RRDN exhibit comparable performance to the DSC/MS and RRDN, respectively (Fig. 6). This result indicates that imposing the equivariance does not necessarily result in the deterioration of the accuracy of SR.

The smaller number of parameters suggests that an equivariant model is trainable with a smaller size of data.¹⁶ Figure 7 shows the dependency of NER (15) on the training data size. The subsampled LR velocity was used here; a similar figure

TABLE I. Numbers of the trainable parameters in the super-resolution models. The C_4 -equivariant DSC/MS and RRDN are used in the decaying turbulence experiment (Section V A) and the C_2 -equivariant ones are used in the barotropic instability experiment (Section V B).

Model name	Number of trainable parameters
DSC/MS	141,298
C_2 -Equivariant DSC/MS	37,128
C_4 -Equivariant DSC/MS	18,564
RRDN	1,256,770
C_2 -Equivariant RRDN	419,104
C_4 -Equivariant RRDN	209,552

was obtained with the averaged data. With the increase in the data size, the NER tends to decrease for all SR models. The NERs of the equivariant models (solid lines) are smaller than those of the original ones (dashed lines), and the difference in the NER tends to be larger as the data size is decreased. Therefore, if only a small size of data is available, an equivariant model should be used.

The equivariance is finally examined. The square flat torus possesses the rotational symmetry in multiples of 90° ; hence, the EER (17) should be zero at these angles. Figure 8 shows the EERs against the various rotation angles. The subsampled velocity with the scale factor $s = 9$ was super-resolved here; similar figures were obtained in the other cases. The Eq-DSC/MS and Eq-RRDN show quite small EERs ($\sim 10^{-7}$) at the multiples of 90° [Fig. 8(a)], which confirms that both models are C_4 -equivariant. The original models, i.e., the DSC/MS and RRDN, show smaller EERs at the multiples of 90° than those at the other angles [Fig. 8(b)]. The magnitude of these EERs is approximately 10^{-2} and is nearly the same as those of NERs in Fig. 6. Therefore, in practice, it is difficult to distinguish between the SR errors and equivariance errors. This result explains why the errors between the equivariant and original models are not largely different in Fig. 6. The conventional CNNs, namely the DSC/MS and RRDN, have learned the C_4 -equivariance from the training data.

In summary, the main advantage of the equivariant SR models is the trainability with a smaller size of the data. The accuracy was not significantly improved by imposing the equivariance as prior knowledge. This result is in contrast to those of the previous studies that apply the equivariant NNs to the modeling of the Reynolds stress tensors^{17,18,70} or governing equations.^{14,15} A possible reason is that the conventional CNNs learn the equivariance from the training data. This result implies that trained CNNs can recognize vector directions because the equivariance leads to the covariance, which distinguishes between scalar and vector.

B. Barotropic instability experiment

This subsection briefly discusses the results of the barotropic instability experiment. The results are similar to those of the decaying turbulence in the previous subsection.

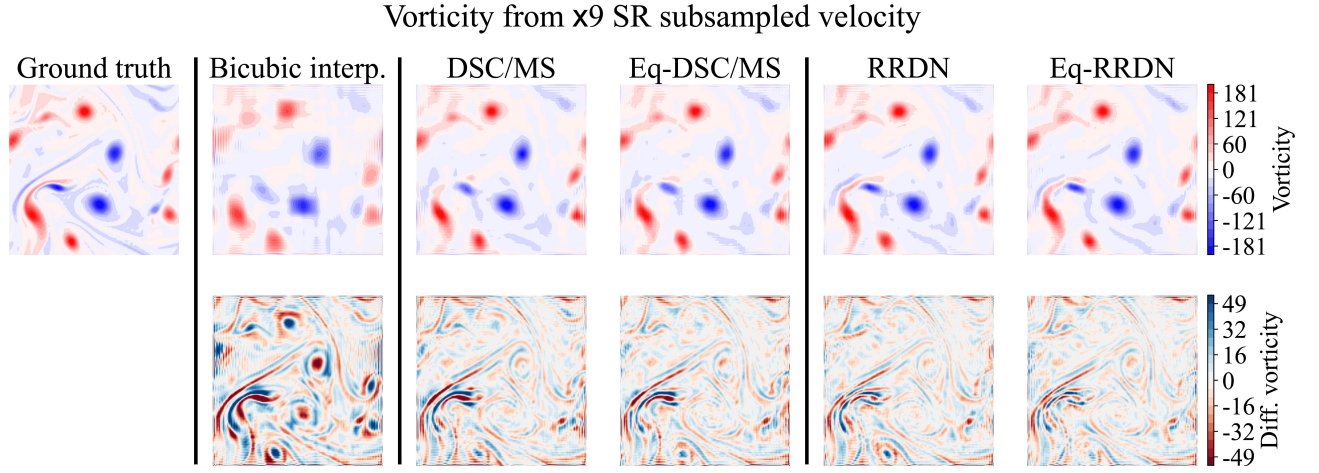


FIG. 5. An example of the vorticity calculated from the inferred velocity in the decaying turbulence. The subsampled low-resolution velocity was super-resolved with the scale factor $s = 9$. The label “Bicubic interp.” means bicubic interpolation. The bottom row shows the difference from the ground truth.

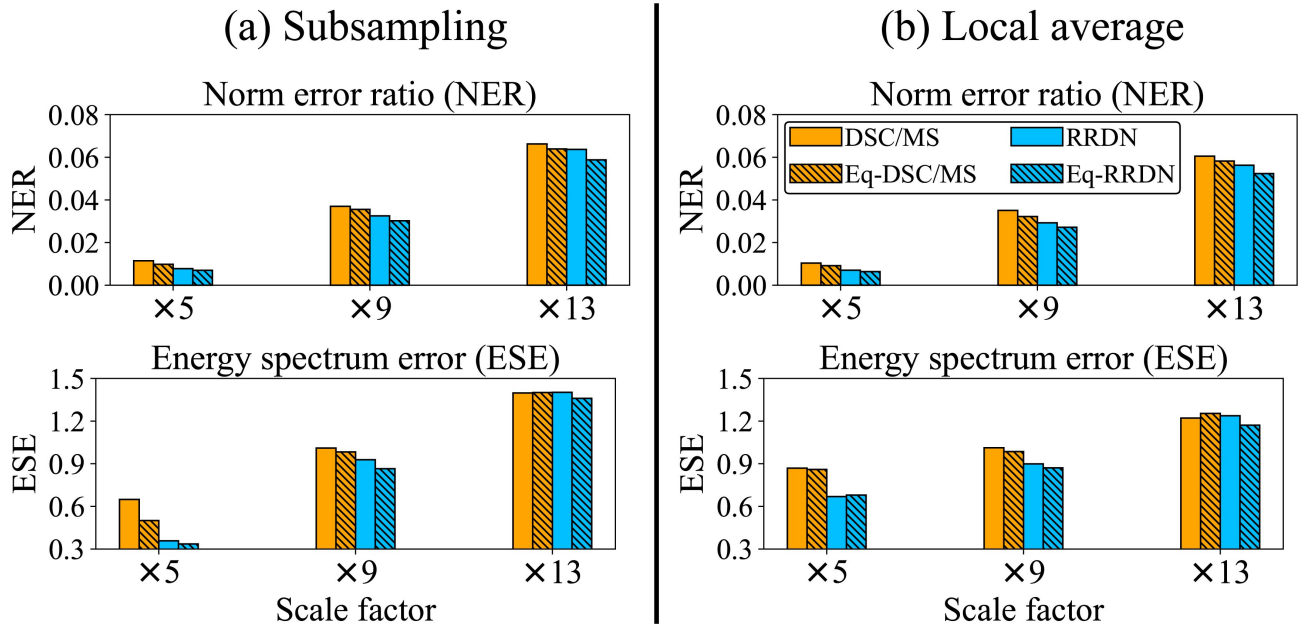


FIG. 6. Test scores calculated from the inferred velocity in the decaying turbulence. The low-resolution velocity is generated with (a) the subsampling and (b) the local average. The norm error ratio (NER) and energy spectrum error (ESE) are defined in (15) and (16), respectively.

The main difference stems from the fact that the periodic channel exhibits the rotational symmetry in 180° . The original DSC/MS and RRDN learn the C_2 -equivariance and are compared with the C_2 -equivariant Eq-DSC/MS and Eq-RRDN.

Figure 9 shows an example of the vorticity calculated from the super-resolved velocity. The vortices obtained with the bicubic interpolation have indistinct shapes. In contrast, all SR models reproduce well the cat’s eye structure⁷⁶ associated with the collapse of the laminar flow having the strong shear. The flows inferred by the equivariant models are nearly the same as those by the original ones.

Figure 10 compares the NERs (15) and ESEs (16) from the SR of the subsampled and locally averaged velocity. The fig-

ure suggests that the Eq-DSC/MS and Eq-RRDN are as accurate as the DSC/MS and RRDN, respectively. The Eq-RRDN and RRDN tend to exhibit lower errors than the Eq-DSC/MS and DSC/MS, respectively, as in the case of the decaying turbulence (Fig. 6).

Figure 11 shows the EERs (17) against the various rotation angles. The subsampled velocity with the scale factor $s = 9$ was super-resolved here; similar figures were obtained in the other cases. The Eq-DSC/MS and Eq-RRDN show quite small EERs ($\sim 10^{-7}$) at 180° [Fig. 11(a)], which is consistent with the imposed C_2 -equivariance. The original models, i.e., DSC/MS and RRDN, learn the C_2 -equivariance [Fig. 11(b)]; the magnitude of EERs at 180° is on the order of 10^{-2}

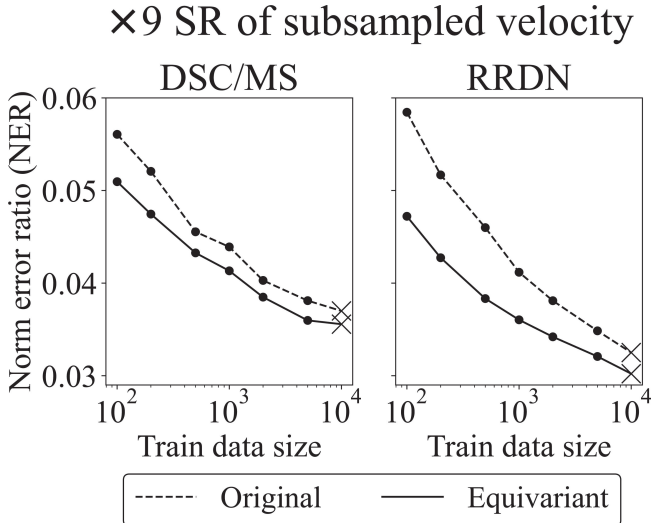


FIG. 7. Norm error ratios (NERs) against various sizes of the training data of the decaying turbulence. The NER in (15) was calculated using the same test data in all cases. The subsampled low-resolution velocity was super-resolved with the scale factor $s = 9$. The train data size means the number of snapshots used in optimizing the SR models, where 30% of the data was used for the validation. The crosses stand for the configurations used in Fig. 6.

and is nearly the same as those of NERs in Fig. 10. In practice, it is difficult again to distinguish between the SR errors and equivariance errors. Differently from the decaying turbulence [Fig. 8(b)], the EERs of the DSC/MS and RRDN are not small at 90° and 270° [Fig. 11(b)]. This result indicates that the learned equivariance reflects the rotational symmetry of the fluid system. We confirmed that the accuracy is not largely improved when the higher-order equivariance such as C_4 is imposed on the Eq-DSC/MS and Eq-RRDN. Therefore, the equivariance reflecting the rotational symmetry of a fluid system should be imposed on an SR model.

C. Equivariance breaking due to data generation

The C_4 -equivariance has been imposed on the Eq-DSC/MS and Eq-RRDN in the decaying turbulence because the fluid system possesses the rotational symmetry in multiples of 90° . Even if the equivariance is not imposed as prior knowledge, the original DSC/MS and RRDN can learn the C_4 -equivariance from the training data [Fig. 8(b)]. Those results imply that the data themselves reflect the rotational symmetry of the fluid system. However, this symmetry can be broken, depending on the method of data generation.

Figure 12 is a schematic that compares the subsampling of the scale factor $s = 2$ and 3. The LR image for $s = 2$, generated by subsampling, is varied via the orientation of the HR image, whereas the LR image for $s = 3$ is not. In the former case, the local correspondence between LR and HR patterns depends on the orientation. Mathematically, the subsampling of an even number s is not commutative with the rotation in

multiples of 90° . This statement is formulated by

$$(d \circ g)(Y) \neq (g \circ d)(Y), \quad (18)$$

where d is the subsampling operation, g is the representation of a rotation in multiples of 90° [Eq. (3)], and Y is an HR velocity field. The input LR field is given by $X = d(Y)$.

The C_4 -equivariance is broken by the non-commutativity of subsampling (18). Consider an HR velocity Y and its rotated version $g(Y)$, both of which can exist because the flow system has the rotational symmetry. The LR fields are generated as $X = d(Y)$ and $X' = d(g(Y))$. Importantly, X' is not equal to $g(X)$ [$= g(d(Y))$]. The non-commutativity results in the inconsistency of LR and HR pairs. When an SR model is trained with the pairs of (X, Y) and $(X', g(Y))$, it fails to learn the equivariance because $(X', g(Y))$ is not $(g(X), g(Y))$. Thus, in this case, the C_4 -equivariance should not be imposed on SR models.

The effect of the non-commutativity (18) is demonstrated by comparing the test scores from the super-resolved velocities of $s = 4$ and 5 (Fig. 13). The NERs (15) and ESEs (16) of the equivariant models are clearly greater than those of the original models, in the case of subsampling of $s = 4$ (Fig. 13[a]); in particular, the NERs of the Eq-DSC/MS and Eq-RRDN are approximately four times larger. In contrast, when $s = 5$ such large errors are not observed because the subsampling is commutative with the rotation. As for the local average, the downsampling is always commutative with the rotation regardless of s , and large errors are not found in both cases of $s = 4$ and 5 (Fig. 13[b]). The result implies that the SR model deteriorates if the equivariance is forcefully imposed when the data do not have rotational symmetry.

Figure 14 shows an example of the vorticity calculated from the super-resolved velocity, where the LR velocity was generated with the subsampling of $s = 4$. The error from the ground truth is larger in the inferred fields of the Eq-DSC/MS and Eq-RRDN than in those of the DSC/MS and RRDN, respectively. This result is in contrast to Fig 5, where $s = 9$ and the inferred fields by all SR models are nearly the same.

Figure 15 shows the curves of EER (17) for the original models, i.e., the DSC/MS and RRDN, with $s = 4$ and 5. In the case of the local average [Fig. 15(a)], the EERs are small at multiples of 90° regardless of s , indicating that the DSC/MS and RRDN learn the C_4 -equivariance. In contrast, in the case of subsampling [Fig. 15(b)], the C_4 -equivariance is learned only when $s = 5$ (solid curves) and not when $s = 4$ (dashed curves). This result suggests that the data do not have rotational symmetry in the latter case.

Even if a fluid system has rotational symmetry, this symmetry may not carry over to pairs of LR and HR velocity. An SR model trained with these inconsistent data is not equivariant. If the coordinates are rotated (i.e., a passive transform), both LR and HR velocities are rotated in the same manner. However, as the SR model is not equivariant, the super-resolved velocity is not rotated according to a rotation of the input. Consequently, the output velocity does not satisfy the covariance to rotation and cannot be regarded as a geometric vector. In this case, the accuracy of a CNN may deteriorate if the equivariance is forcefully imposed as prior knowledge. Instead of

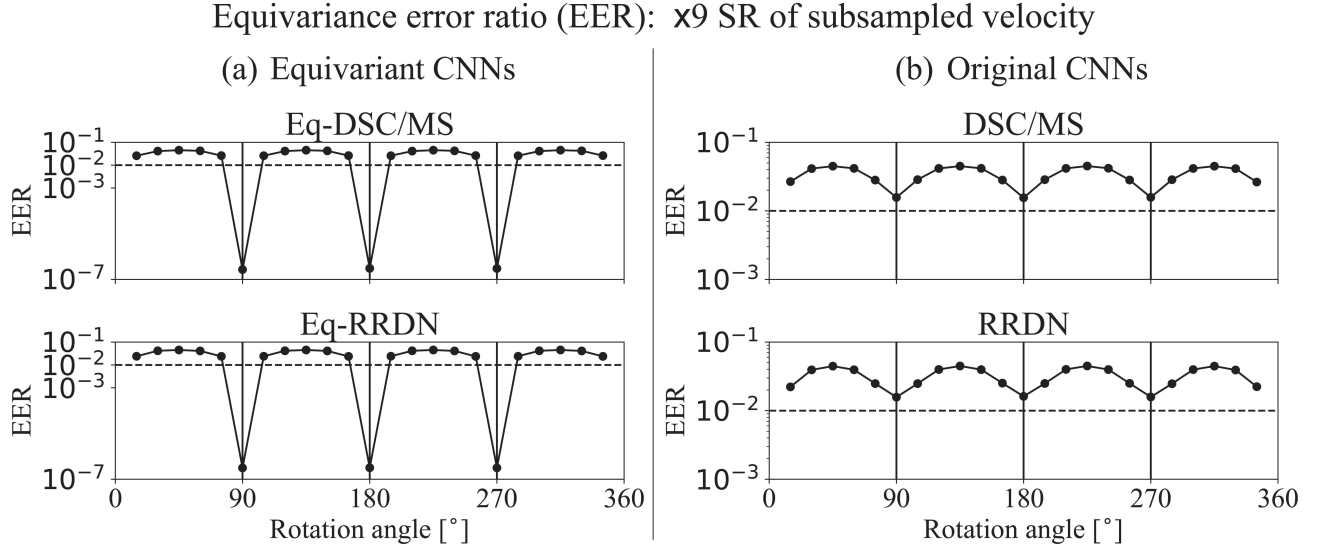


FIG. 8. Equivariance error ratio (EER) against the rotation angle in the decaying turbulence. The EER is defined in (17). The subsampled low-resolution velocity was super-resolved with the scale factor $s = 9$. The rotation angle interval is 15° , where 0° and 360° are omitted. The horizontal dashed lines show $EER = 10^{-2}$ in all sub-figures.

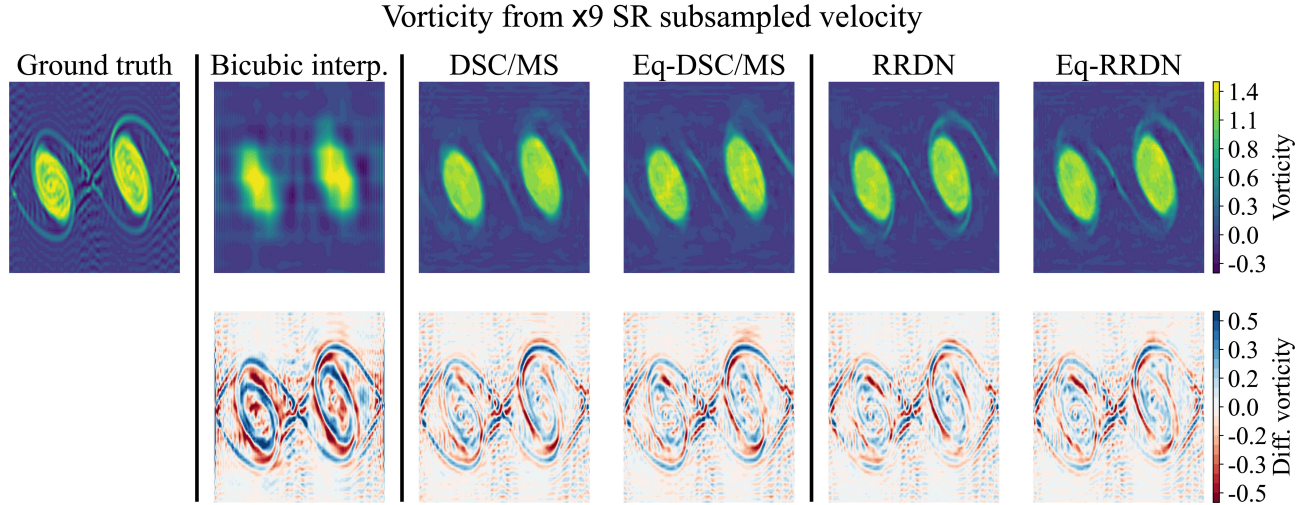


FIG. 9. An example of the vorticity calculated from the inferred velocity in the barotropic instability. The subsampled low-resolution velocity was super-resolved with the scale factor $s = 9$. The label “Bicubic interp.” means bicubic interpolation. The bottom row shows the difference from the ground truth.

the equivariant CNNs, the conventional CNNs should be used, in which vector is treated like scalar, because the data themselves do not have rotational symmetry. Most importantly, the conventional CNNs can learn the equivariance, adapting to the symmetry of data. In contrast, the equivariant CNNs do not have this flexibility and their inference can be sensitive to the method of data generation.

VI. CONCLUSIONS

Vector is an essential quantity in physics. In applications of convolutional neural networks (CNNs), however, vectors

are often apparently processed as quantities having no direction such as colors in images. This study has investigated the effect of treating vector as a geometric quantity, wherein a direction is recognized in terms of super-resolution (SR) of two-dimensional flows. Vector can be distinguished from scalar by the transformation law, that is, the covariance in geometry.^{8,9} The equivariant CNNs^{50,58–60} can incorporate the transformation laws as prior knowledge and preserve the covariance of vector regardless of training. In this paper, the two existing CNNs^{25,32} are converted into equivariant ones using a theory of equivariant deep learning,⁶⁰ where the rotation and translation equivariance are considered. The CNNs were trained with the pairs of high- and low-resolution (HR and LR) velocities.

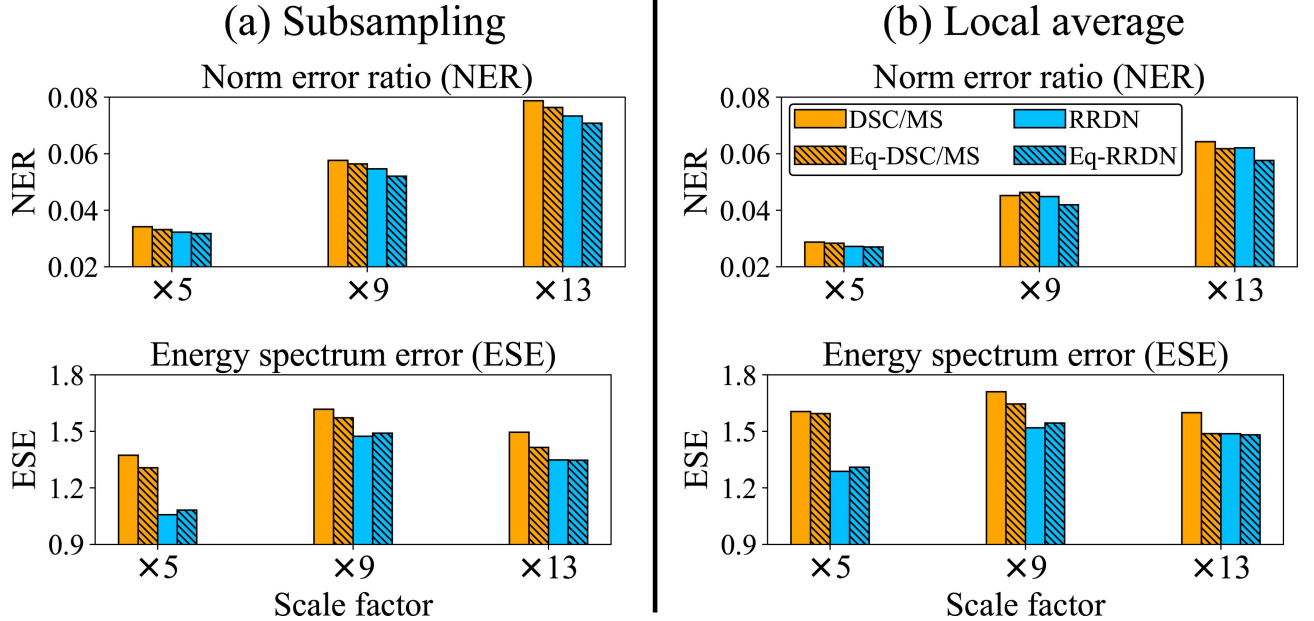


FIG. 10. Test scores calculated from the inferred velocity in the barotropic instability. The low-resolution velocity is generated with (a) the subsampling and (b) the local average. The norm error ratio (NER) and energy spectrum error (ESE) are defined in (15) and (16), respectively.

Equivariance error ratio (EER): $\times 9$ SR of subsampled velocity

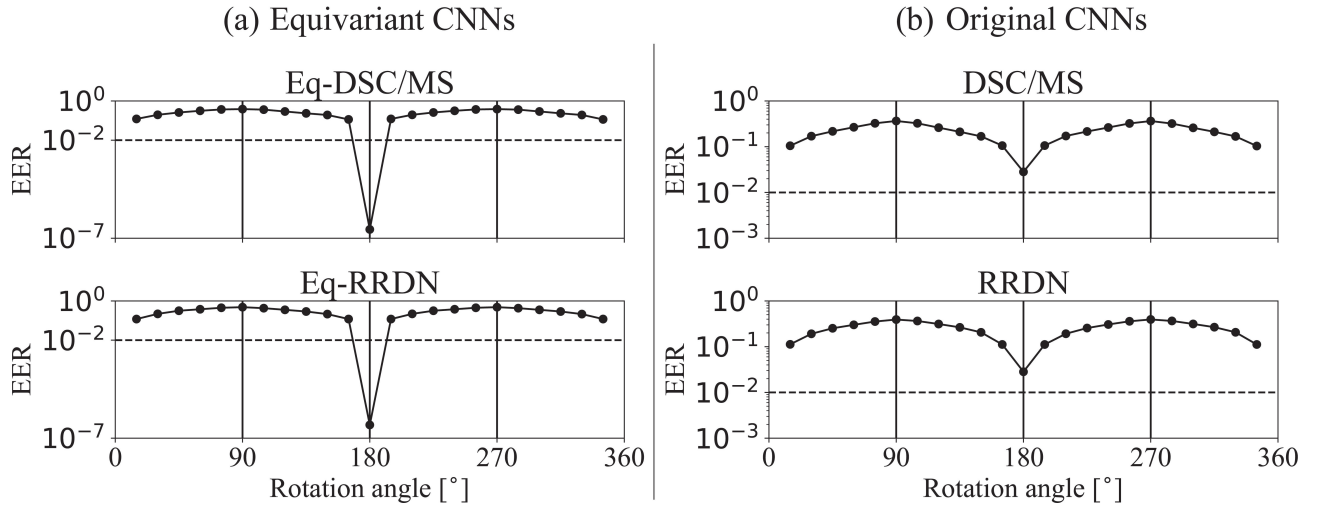


FIG. 11. Equivariance error ratio (EER) against the rotation angle in the barotropic instability. The EER is defined in (17). The subsampled low-resolution velocity was super-resolved with the scale factor $s = 9$. The rotation angle interval is 15° , where 0° and 360° are omitted. The horizontal dashed lines show $EER = 10^{-2}$ in all sub-figures.

The HR velocity was generated from the two-dimensional fluid dynamics simulations, whereas the LR velocity was obtained by downsampling, i.e., either subsampling or local averaging.

The contrasting results have been obtained depending on the symmetry of the data. When the data reflect the rotational symmetry of the fluid system, the equivariant CNNs exhibit comparable accuracy with that of the conventional ones, which is likely because the conventional CNNs learn the equivariance from the training data. In this case, not only

the equivariant CNNs but also the conventional ones recognize vector directions (i.e., the covariance). On the other hand, when the rotational symmetry of the data is broken, the accuracy of the equivariant CNNs is lower than that of the conventional ones. This symmetry breaking can easily occur when the resolution of the LR velocity is varied. In this case, the orientation of the data must be fixed and vector is treated as a tuple of scalars having no direction.

In conclusion, the equivariant CNNs do not show a significant improvement in accuracy or the robustness of infer-

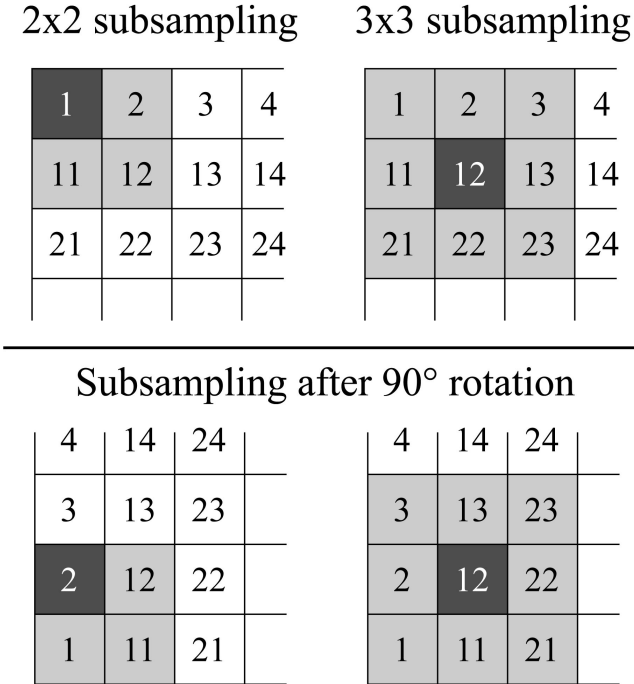


FIG. 12. Schematic showing the commutative property of subsampling with rotation. (left) When the scale factor $s = 2$, the subsampling picks up the upper left pixels (black tiles) in the 2×2 windows. (right) When $s = 3$, the central pixels are extracted regardless of the orientation.

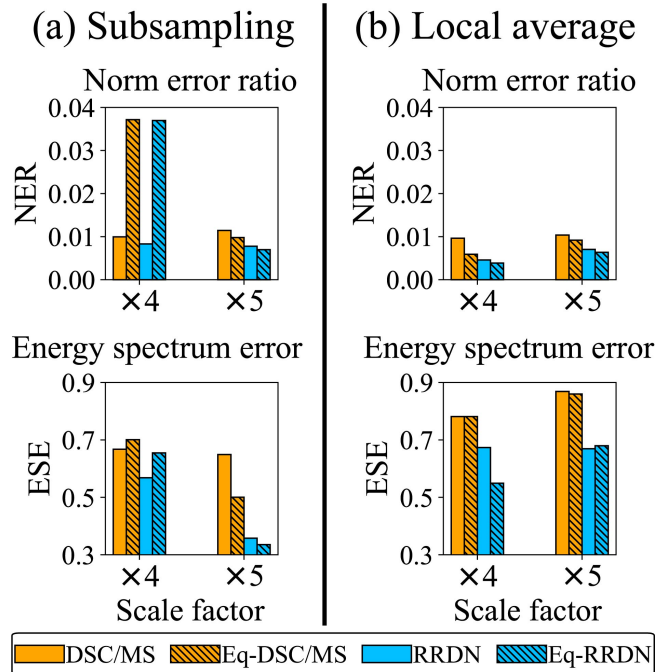


FIG. 13. Test scores calculated from the inferred velocity in the decaying turbulence. The low-resolution velocity was generated with (a) the subsampling and (b) the local average. The norm error ratio (NER) and energy spectrum error (ESE) are defined in (15) and (16), respectively. All scores of the scale factor $s = 5$ are the same as those in Fig. 6.

ence in the super-resolution task of the two-dimensional fluids. This conclusion is in contrast to the results of the previous studies^{13–18} that apply equivariant neural networks to fluids. The main advantage of equivariant CNNs found in this paper is the trainability with a smaller size of data due to the reduction in the parameters.

There are at least two directions to future work. The first is the investigation of other equivariance. The Galilean^{14,70} or scale equivariance^{14,57} may be important for fluid systems. The second is the SR on irregular coordinates. The present paper has utilized the Cartesian coordinates, where the basis vectors are the same at all locations. Generally, convolution employs the parallel transform of vectors and the difference in basis needs to be incorporated.^{82,83} Although the present paper does not find major advantages in using equivariant CNNs, this conclusion may depend on the configuration of coordinate systems. Geophysical fluids may be appropriate to examine the dependency of SR on coordinates because oceanic or atmospheric flows are often described with latitudes and longitudes, which compose non-equally spaced grids.

ACKNOWLEDGMENTS

This work was supported by the JSPS KAKENHI (grant number 20H05751). The deep learning was conducted on the supercomputer of TSUBAME 3.0 at the Tokyo Institute of Technology. We would like to thank Editage (www.editage.com) for English language editing.

DATA AVAILABILITY STATEMENT

The data that support the findings of this study are available within the article. The source code is available on the GitHub repository.⁷¹

Appendix A: Dependency on the order of cyclic groups

An important hyper-parameter of equivariant CNNs is the order N of a cyclic group C_N as discussed in Sections III B and IV C. This section investigates the dependency of test scores on N by using the decaying turbulence data. The test errors do not necessarily decrease as N is increased, which is in contrast to the result in image classification.^{52,56,60}

The effect of changing the order of C_N is first examined for the Eq-DSC/MS. This model has various spatial sizes of kernels in the hidden layers (Fig. 3), all of which were fixed here. In each layer, the number of sets of the regular representation was also fixed. For instance, if both input and output of a hidden layer are composed of two sets of the regular representation, the number of the channels is 16 for C_8 and 24 for C_{12} . In this preference, as N is increased, the number of trainable parameters increases. Figure 16 shows the NERs (15) and ESEs (16) of C_4 , C_8 , and C_{12} . Both NER and ESE are the minima in the case of C_8 , and the scores are not strongly decreased by increasing the order of C_N .

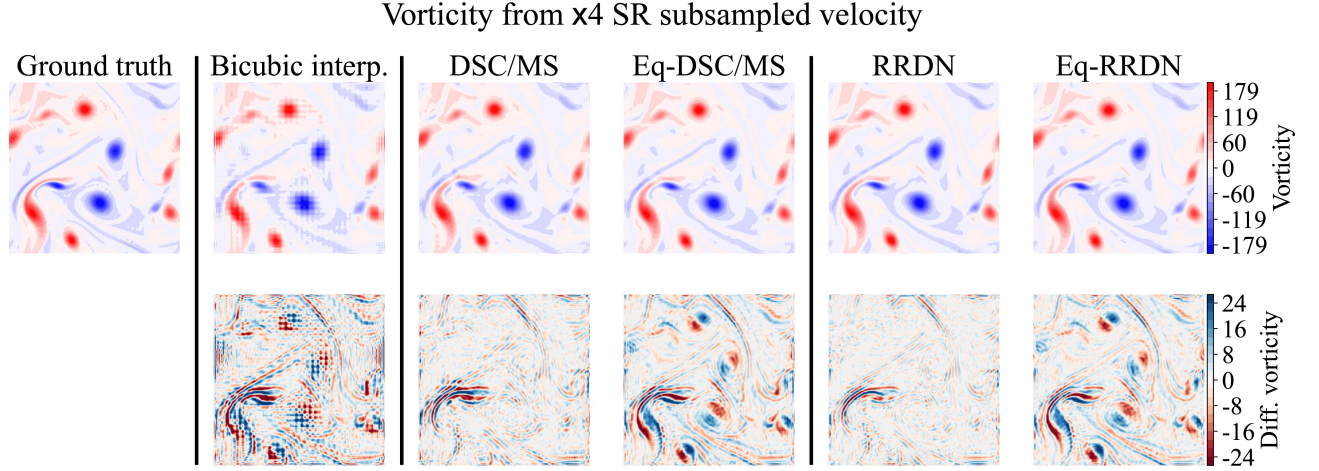


FIG. 14. An example of the vorticity calculated from the inferred velocity in the decaying turbulence. The subsampled low-resolution velocity was super-resolved with the scale factor $s = 4$. The label “Bicubic interp.” means bicubic interpolation. The bottom row shows the difference from the ground truth.

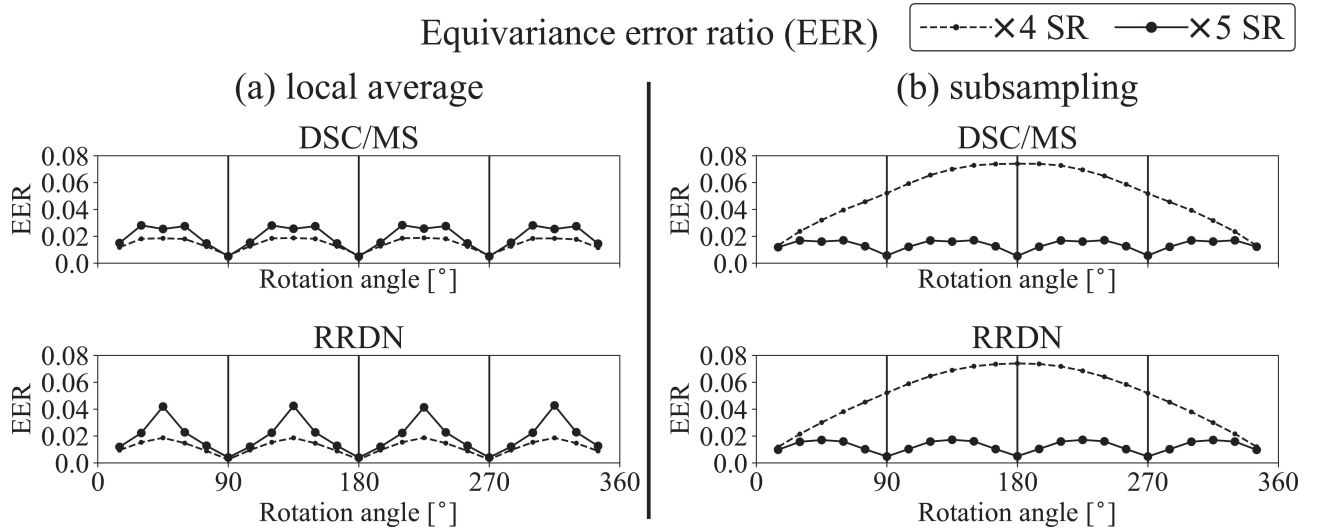


FIG. 15. Equivariance error ratio (EER) against the rotation angle for the DSC/MS and RRDN. The EER is defined in (17). The low-resolution velocity was generated with (a) the local average and (b) the subsampling, where the scale factor $s = 4$ or 5. The interval of rotation angle is 15° , where 0° and 360° are omitted.

The spatial size of kernels usually needs to be larger when the order of C_N is increased because the interpolation is used to determine the kernel pattern.^{53,60} The Eq-RRDN is appropriate for an experiment varying both C_N and kernel size because all kernels have the same spatial size (Fig 4). The Eq-RRDN consisting of one dense block (Fig. 4) was employed here to reduce the training cost. Each hidden layer utilizes eight sets of the regular representation. For instance, the number of the channels is 32 for C_4 and 96 for C_{12} . As N is increased, the number of trainable parameters increases again. Figure 17 shows the NERs (15) and ESEs (16) against the various C_N and spatial sizes of kernels. The error reduction by increasing N is not as strong as that by increasing the kernel size.

The above results may be attributed to the long-range in-

teraction nature of two-dimensional fluids.⁸⁴ Due to this nature, not only global but also local distribution of vortices is affected by the shapes of distant vortices and boundaries. Furthermore, the boundary condition of the decaying turbulence is symmetric to the global rotation in multiples of 90° . These facts imply that imposing the C_4 -equivariance is sufficient.

Appendix B: Comparison between the super-resolution of velocity and vorticity

The SR of velocity has been discussed. Similar results were obtained in the SR of vorticity. The former is referred to as the velocity-SR and the latter as the vorticity-SR. This section compares the velocity-SR with the vorticity-SR by using the

Eq-DSC/MS: $\times 9$ SR of subsampled velocity

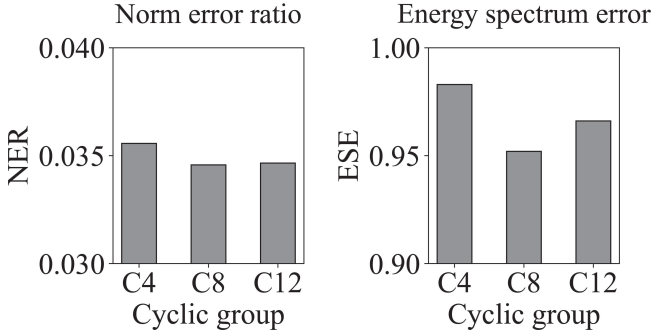


FIG. 16. Test scores against the orders of cyclic group C_N used in the Eq-DSC/MS. The subsampled velocity from the decaying turbulence was super-resolved with the scale factor $s = 9$. The NER (norm error ratio) and ESE (energy spectrum error) are defined in (15) and (16), respectively.

Eq-RRDN: $\times 9$ SR of subsampled velocity

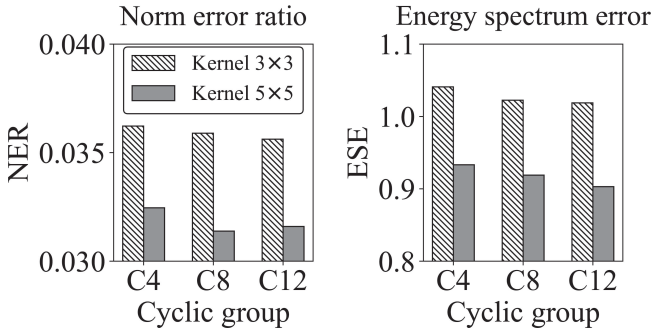


FIG. 17. Test scores against the various C_N and kernel sizes used in the Eq-RRDN. The subsampled velocity from the decaying turbulence was super-resolved with the scale factor $s = 9$. The NER (norm error ratio) and ESE (energy spectrum error) are defined in (15) and (16), respectively.

decaying turbulence data.

Figure 18 compares the test scores between the velocity-SR and vorticity-SR. The scale factor is $s = 9$ here. The NER (15) in Fig. 18 evaluates the inferred vorticity, where in the SR of velocity it was calculated from the velocity with the discrete Fourier transform. Furthermore, the vorticity spectrum error (VSE) is shown in Fig. 18 instead of the ESE. The VSE is defined as (16), where the energy spectra are replaced with the enstrophy spectra. The NERs are comparable between the velocity-SR and vorticity-SR: the difference in the NER is limited to approximately 10%. In contrast, the VSEs of the velocity-SR are approximately twice as small as those of the vorticity-SR, implying that the velocity-SR is more valid.

Figure 19 compares the energy and enstrophy spectra between the velocity-SR and vorticity-SR. Only the results of the Eq-DSC/MS and Eq-RRDN are shown because the DSC/MS and RRDN yielded almost the same spectra. The velocity-SR well reproduces the energy and enstrophy spectra over the middle range of wavenumbers $10 \lesssim k \lesssim 25$, compared to

those of the vorticity-SR. This result is consistent with the VSE values in Fig. 18. Therefore, it can be concluded that the velocity-SR is more physically valid than the vorticity-SR. Although a direct comparison between the velocity-SR and vorticity-SR is not found in Ref. 25, it reports that the L_2 norm error is smaller in the super-resolved velocity than in the super-resolved vorticity. Our result is consistent with theirs.

The lower accuracy of the vorticity-SR may not be attributed to the difference between scalar and vector. The equivariant models incorporate the transformation law of scalars or vectors, which assures that the vorticity calculated from the super-resolved velocity is a scalar field. Vorticity fields generally have finer structures than velocity fields owing to the differential operation. The difference in spatial scales might cause a difference in the accuracy of SR.

- ¹S. L. Brunton, B. R. Noack, and P. Koumoutsakos, “Machine learning for fluid mechanics,” *Annual Review of Fluid Mechanics* **52**, 477–508 (2020), <https://doi.org/10.1146/annurev-fluid-010719-060214>.
- ²K. Duraisamy, “Perspectives on machine learning-augmented reynolds-averaged and large eddy simulation models of turbulence,” *Phys. Rev. Fluids* **6**, 050504 (2021).
- ³R. Vinuesa and S. L. Brunton, “The potential of machine learning to enhance computational fluid dynamics,” (2021), arXiv:2110.02085 [physics.flu-dyn].
- ⁴S. L. Brunton, “Applying machine learning to study fluid mechanics,” *Acta Mechanica Sinica* (2022), 10.1007/s10409-021-01143-6.
- ⁵M. Raissi, P. Perdikaris, and G. Karniadakis, “Physics-informed neural networks: A deep learning framework for solving forward and inverse problems involving nonlinear partial differential equations,” *Journal of Computational Physics* **378**, 686–707 (2019).
- ⁶K. Kashinath, M. Mustafa, A. Albert, J.-L. Wu, C. Jiang, S. Esmaeilzadeh, K. Azizzadenesheli, R. Wang, A. Chattopadhyay, A. Singh, A. Manepalli, D. Chirila, R. Yu, R. Walters, B. White, H. Xiao, H. A. Tchelepi, P. Marcus, A. Anandkumar, P. Hassanzadeh, and n. Prabhat, “Physics-informed machine learning: case studies for weather and climate modelling,” *Philosophical Transactions of the Royal Society A: Mathematical, Physical and Engineering Sciences* **379**, 20200093 (2021), <https://royalsocietypublishing.org/doi/pdf/10.1098/rsta.2020.0093>.
- ⁷S. Cai, Z. Mao, Z. Wang, M. Yin, George, and E. Karniadakis, “Physics-informed neural networks (pinns) for fluid mechanics: a review,” *Acta Mechanica Sinica* (2022), 10.1007/s10409-021-01148-1.
- ⁸B. F. Schutz, *Geometrical Methods of Mathematical Physics*, first edition ed. (Cambridge University Press, 1980).
- ⁹M. Nakahara, *Geometry, Topology and Physics*, second edition ed. (CRC Press, 2003).
- ¹⁰P. A. M. Dirac, *General Theory of Relativity* (Princeton University Press, 1996).
- ¹¹M. M. Bronstein, J. Bruna, T. Cohen, and P. Veličković, “Geometric deep learning: Grids, groups, graphs, geodesics, and gauges,” *CoRR abs/2104.13478* (2021), 2104.13478.
- ¹²K. Atz, F. Grisoni, and G. Schneider, “Geometric deep learning on molecular representations,” *Nature Machine Intelligence* **3**, 1023–1032 (2021).
- ¹³L. Gao, Y. Du, H. Li, and G. Lin, “Roteqnet: Rotation-equivariant network for fluid systems with symmetric high-order tensors,” *CoRR abs/2005.04286* (2020), 2005.04286.
- ¹⁴R. Wang, R. Walters, and R. Yu, “Incorporating symmetry into deep dynamics models for improved generalization,” (2021).
- ¹⁵J. Suk, P. de Haan, P. Lippe, C. Brune, and J. M. Wolterink, “Equivariant graph neural networks as surrogate for computational fluid dynamics in 3d artery models,” in *Fourth Workshop on Machine Learning and the Physical Sciences (NeurIPS 2021)*. (2021).
- ¹⁶B. Siddani, S. Balachandar, and R. Fang, “Rotational and reflectional equivariant convolutional neural network for data-limited applications: Multiphase flow demonstration,” *Physics of Fluids* **33**, 103323 (2021), <https://doi.org/10.1063/5.0066049>.
- ¹⁷J. Han, X.-H. Zhou, and H. Xiao, “Vcnn-e: A vector-cloud neural net-

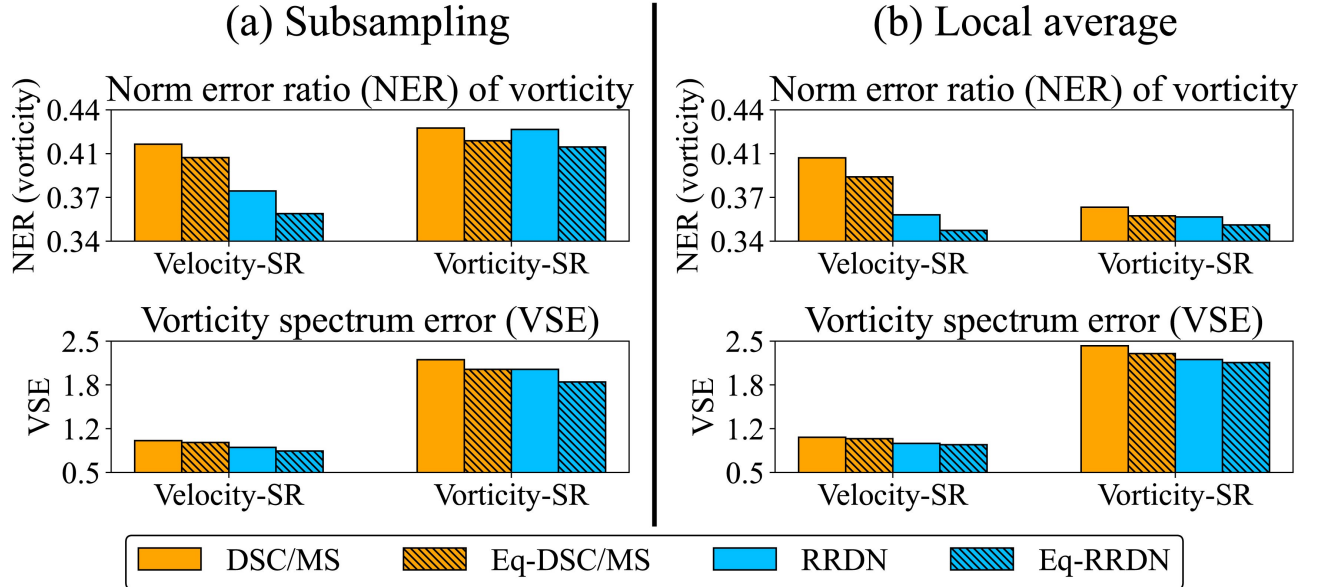


FIG. 18. Test scores calculated from the inferred flow fields in the decaying turbulence. The low-resolution data of the scale factor $s = 9$ were generated with (a) the subsampling and (b) the local average. The label “Velocity-SR” (“Vorticity-SR”) means that the velocity (vorticity) is directly super-resolved. The NER is defined in (15), where the vorticity is evaluated in all cases. The VSE is defined as (16), where the energy spectra are replaced with the enstrophy spectra.

work with equivariance for emulating reynolds stress transport equations,” (2022), arXiv:2201.01287 [physics.flu-dyn].

¹⁸S. Pawar, O. San, A. Rasheed, and P. Vedula, “Frame invariant neural network closures for kraichnan turbulence,” (2022), arXiv:2201.02928 [physics.flu-dyn].

¹⁹C. Dong, C. C. Loy, K. He, and X. Tang, “Learning a deep convolutional network for image super-resolution,” in *Computer Vision – ECCV 2014*, edited by D. Fleet, T. Pajdla, B. Schiele, and T. Tuytelaars (Springer International Publishing, Cham, 2014) pp. 184–199.

²⁰C. Ledig, L. Theis, F. Huszar, J. Caballero, A. Cunningham, A. Acosta, A. Aitken, A. Tejani, J. Totz, Z. Wang, and W. Shi, “Photo-realistic single image super-resolution using a generative adversarial network,” in *Proceedings of the IEEE Conference on Computer Vision and Pattern Recognition (CVPR)* (2017).

²¹X. Wang, K. Yu, S. Wu, J. Gu, Y. Liu, C. Dong, Y. Qiao, and C. Change Loy, “EsrGAN: Enhanced super-resolution generative adversarial networks,” in *Proceedings of the European Conference on Computer Vision (ECCV) Workshops* (2018).

²²V. K. Ha, J.-C. Ren, X.-Y. Xu, S. Zhao, G. Xie, V. Masero, and A. Hussain, “Deep learning based single image super-resolution: A survey,” *International Journal of Automation and Computing* (2019), 10.1007/s11633-019-1183-x.

²³S. Anwar, S. Khan, and N. Barnes, “A deep journey into super-resolution: A survey,” *ACM Comput. Surv.* **53** (2020), 10.1145/3390462.

²⁴Z. Deng, C. He, Y. Liu, and K. C. Kim, “Super-resolution reconstruction of turbulent velocity fields using a generative adversarial network-based artificial intelligence framework,” *Physics of Fluids* **31** (2019), 10.1063/1.5127031.

²⁵K. Fukami, K. Fukagata, and K. Taira, “Super-resolution reconstruction of turbulent flows with machine learning,” *Journal of Fluid Mechanics* **870**, 106–120 (2019).

²⁶R. Maulik, K. Fukami, N. Ramachandra, K. Fukagata, and K. Taira, “Probabilistic neural networks for fluid flow surrogate modeling and data recovery,” *Phys. Rev. Fluids* **5**, 104401 (2020).

²⁷C. Wang, E. Bentivegna, W. Zhou, L. Klein, and B. Elmegreen, “Physics-informed neural network super resolution for advection-diffusion models,” in *Third Workshop on Machine Learning and the Physical Sciences (NeurIPS 2020)* (2020).

²⁸K. Fukami, K. Fukagata, and K. Taira, “Assessment of supervised machine learning methods for fluid flows,” *Theoretical and Computational Fluid Dynamics* **34**, 497–519 (2020).

²⁹K. Fukami, K. Fukagata, and K. Taira, “Machine-learning-based spatio-temporal super resolution reconstruction of turbulent flows,” *Journal of Fluid Mechanics* **909**, A9 (2021).

³⁰L. Wang, Z. Luo, J. Xu, W. Luo, and J. Yuan, “A novel framework for cost-effectively reconstructing the global flow field by super-resolution,” *Physics of Fluids* **33**, 095105 (2021), <https://doi.org/10.1063/5.0062775>.

³¹B. Liu, J. Tang, H. Huang, and X.-Y. Lu, “Deep learning methods for super-resolution reconstruction of turbulent flows,” *Physics of Fluids* **32**, 025105 (2020).

³²M. Bode, M. Gauding, Z. Lian, D. Denker, M. Davidovic, K. Kleinheinz, J. Jitsev, and H. Pitsch, “Using physics-informed enhanced super-resolution generative adversarial networks for subfilter modeling in turbulent reactive flows,” *Proceedings of the Combustion Institute* **38**, 2617–2625 (2021).

³³H. Kim, J. Kim, S. Won, and C. Lee, “Unsupervised deep learning for super-resolution reconstruction of turbulence,” *Journal of Fluid Mechanics* **910**, A29 (2021).

³⁴C. Jiang, S. Esmaeilzadeh, K. Azizzadenesheli, K. Kashinath, M. Mustafa, H. A. Tchelepi, P. Marcus, M. Prabhat, and A. Anandkumar, “Mesh-freeflownet: A physics-constrained deep continuous space-time super-resolution framework,” in *2020 SC20: International Conference for High Performance Computing, Networking, Storage and Analysis (SC)* (IEEE Computer Society, Los Alamitos, CA, USA, 2020) pp. 1–15.

³⁵Y. Xie, E. Franz, M. Chu, and N. Thuerey, “Tempogan: A temporally coherent, volumetric gan for super-resolution fluid flow,” *ACM Trans. Graph.* **37** (2018), 10.1145/3197517.3201304.

³⁶M. Werhahn, Y. Xie, M. Chu, and N. Thuerey, “A multi-pass gan for fluid flow super-resolution,” *Proc. ACM Comput. Graph. Interact. Tech.* **2** (2019), 10.1145/3340251.

³⁷K. Bai, W. Li, M. Desbrun, and X. Liu, “Dynamic upsampling of smoke through dictionary-based learning,” *ACM Trans. Graph.* **40** (2020), 10.1145/3412360.

³⁸E. Ferdinand, A. Suinesiaputra, D. J. Dubowitz, D. Zhao, A. Wang, B. Cowan, and A. A. Young, “4dflownet: Super-resolution 4d flow mri using deep learning and computational fluid dynamics,” *Frontiers in Physics* **8**, 138 (2020).

³⁹L. Sun and J.-X. Wang, “Physics-constrained bayesian neural network for

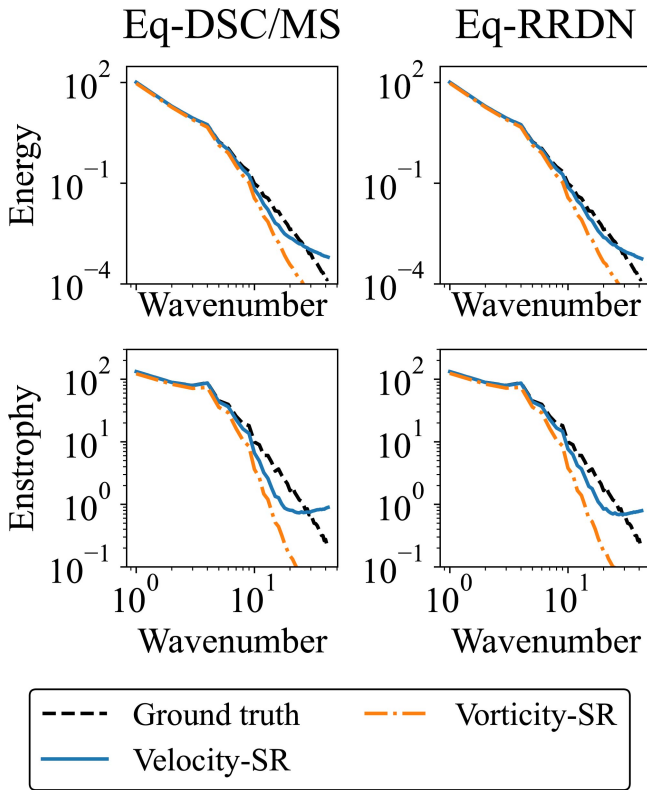


FIG. 19. Ensemble averages of energy and enstrophy spectra at $t = 1.1$ of the decaying turbulence. The time of $t = 1.1$ is the initial time of the test dataset. The label “Velocity-SR” (“Vorticity-SR”) means that the velocity (vorticity) is directly super-resolved. Only the results of the Eq-DSC/MS and Eq-RRDN are shown because the DSC/MS and RRDN yielded almost the same spectra. The scale factor s was nine and the subsampled low-resolution data were used.

fluid flow reconstruction with sparse and noisy data,” *Theoretical and Applied Mechanics Letters* **10**, 161–169 (2020).

⁴⁰H. Gao, L. Sun, and J.-X. Wang, “Super-resolution and denoising of fluid flow using physics-informed convolutional neural networks without high-resolution labels,” *Physics of Fluids* **33**, 073603 (2021).

⁴¹A. Ducournau and R. Fablet, “Deep learning for ocean remote sensing: an application of convolutional neural networks for super-resolution on satellite-derived sst data,” (2016) pp. 1–6.

⁴²A. J. Cannon, “Quantile regression neural networks: Implementation in r and application to precipitation downscaling,” *Computers and Geosciences* **37**, 1277–1284 (2011).

⁴³T. Vandal, E. Kodra, S. Ganguly, A. Michaelis, R. Nemani, and A. R. Ganguly, “Deepsd: Generating high resolution climate change projections through single image super-resolution,” (Association for Computing Machinery, 2017) pp. 1663–1672.

⁴⁴E. R. Rodrigues, I. Oliveira, R. Cunha, and M. Netto, “Deepdownscale: A deep learning strategy for high-resolution weather forecast,” (2018) pp. 415–422.

⁴⁵R. Onishi, D. Sugiyama, and K. Matsuda, “Super-resolution simulation for real-time prediction of urban micrometeorology,” *SOLA* **15**, 178–182 (2019).

⁴⁶J. Leinonen, D. Nerini, and A. Berne, “Stochastic super-resolution for downscaling time-evolving atmospheric fields with a generative adversarial network,” *IEEE Transactions on Geoscience and Remote Sensing* , 1–13 (2020).

⁴⁷K. Stengel, A. Glaws, D. Hettinger, and R. N. King, “Adversarial super-resolution of climatological wind and solar data,” *Proceedings of the National Academy of Sciences* **117**, 16805–16815 (2020).

⁴⁸J. Wang, Z. Liu, I. Foster, W. Chang, R. Kettimuthu, and V. R. Kotamarthi, “Fast and accurate learned multiresolution dynamical downscaling for precipitation,” *Geoscientific Model Development* **14**, 6355–6372 (2021).

⁴⁹Y. Yasuda, R. Onishi, Y. Hirokawa, D. Kolomenskiy, and D. Sugiyama, “Super-resolution of near-surface temperature utilizing physical quantities for real-time prediction of urban micrometeorology,” *Building and Environment* **209**, 108597 (2022).

⁵⁰T. Cohen and M. Welling, “Group equivariant convolutional networks,” in *Proceedings of The 33rd International Conference on Machine Learning*, Proceedings of Machine Learning Research, Vol. 48, edited by M. F. Balcan and K. Q. Weinberger (PMLR, New York, New York, USA, 2016) pp. 2990–2999.

⁵¹T. S. Cohen and M. Welling, “Steerable cnns,” 5th International Conference on Learning Representations, ICLR 2017 (2017).

⁵²D. Marcos, M. Volpi, N. Komodakis, and D. Tuia, “Rotation equivariant vector field networks,” in *Proceedings of the IEEE International Conference on Computer Vision (ICCV)* (2017).

⁵³D. E. Worrall, S. J. Garbin, D. Turmukhambetov, and G. J. Brostow, “Harmonic networks: Deep translation and rotation equivariance,” in *Proceedings of the IEEE Conference on Computer Vision and Pattern Recognition (CVPR)* (2017).

⁵⁴Y. Zhou, Q. Ye, Q. Qiu, and J. Jiao, “Oriented response networks,” in *Proceedings of the IEEE Conference on Computer Vision and Pattern Recognition (CVPR)* (2017).

⁵⁵K. T. Schütt, F. Arbabzadah, S. Chmiela, K. R. Müller, and A. Tkatchenko, “Article quantum-chemical insights from deep tensor neural networks,” *Nature Communications* (2017), 10.1038/ncomms13890.

⁵⁶E. J. Bekkers, M. W. Lafarge, M. Veta, K. A. J. Eppenhof, J. P. W. Pluim, and R. Duits, “Roto-translation covariant convolutional networks for medical image analysis,” in *Medical Image Computing and Computer Assisted Intervention – MICCAI 2018*, edited by A. F. Frangi, J. A. Schnabel, C. Davatzikos, C. Alberola-López, and G. Fichtinger (Springer International Publishing, Cham, 2018) pp. 440–448.

⁵⁷I. Sosnovik, A. Moskalev, and A. W. Smeulders, “Scale equivariance improves siamese tracking,” in *Proceedings of the IEEE/CVF Winter Conference on Applications of Computer Vision (WACV)* (2021) pp. 2765–2774.

⁵⁸R. Kondor and S. Trivedi, “On the generalization of equivariance and convolution in neural networks to the action of compact groups,” in *Proceedings of the 35th International Conference on Machine Learning*, Proceedings of Machine Learning Research, Vol. 80, edited by J. Dy and A. Krause (PMLR, 2018) pp. 2747–2755.

⁵⁹T. S. Cohen, M. Geiger, and M. Weiler, “A general theory of equivariant cnns on homogeneous spaces,” in *Advances in Neural Information Processing Systems*, Vol. 32, edited by H. Wallach, H. Larochelle, A. Beygelzimer, F. d’Alché-Buc, E. Fox, and R. Garnett (Curran Associates, Inc., 2019).

⁶⁰M. Weiler and G. Cesa, “General $e(2)$ -equivariant steerable cnns,” in *Advances in Neural Information Processing Systems*, Vol. 32, edited by H. Wallach, H. Larochelle, A. Beygelzimer, F. d’Alché-Buc, E. Fox, and R. Garnett (Curran Associates, Inc., 2019).

⁶¹R. Gilmore, *Lie Groups, Physics, and Geometry: An Introduction for Physicists, Engineers and Chemists* (Cambridge University Press, 2008).

⁶²A. Zee, *Group Theory in a Nutshell for Physicists* (Princeton University Press, 2016).

⁶³F. Fuchs, D. Worrall, V. Fischer, and M. Welling, “Se(3)-transformers: 3d roto-translation equivariant attention networks,” in *Advances in Neural Information Processing Systems*, Vol. 33, edited by H. Larochelle, M. Ranzato, R. Hadsell, M. F. Balcan, and H. Lin (Curran Associates, Inc., 2020) pp. 1970–1981.

⁶⁴M. Weiler, M. Geiger, M. Welling, W. Boomsma, and T. S. Cohen, “3d steerable cnns: Learning rotationally equivariant features in volumetric data,” in *Advances in Neural Information Processing Systems*, Vol. 31, edited by S. Bengio, H. Wallach, H. Larochelle, K. Grauman, N. Cesa-Bianchi, and R. Garnett (Curran Associates, Inc., 2018).

⁶⁵N. Thomas, T. Smidt, S. M. Kearnes, L. Yang, L. Li, K. Kohlhoff, and P. Riley, “Tensor field networks: Rotation- and translation-equivariant neural networks for 3d point clouds,” *CoRR* **abs/1802.08219** (2018), arXiv:1802.08219.

⁶⁶D. Chen, J. Tachella, and M. E. Davies, “Equivariant imaging: Learning beyond the range space,” in *Proceedings of the IEEE/CVF International Conference on Computer Vision (ICCV)* (2021) pp. 4379–4388.

⁶⁷D. Chen, J. Tachella, and M. E. Davies, “Robust equivariant imaging: a fully unsupervised framework for learning to image from noisy and partial measurements,” CoRR **abs/2111.12855** (2021), 2111.12855.

⁶⁸J. Lee and K. Mu Lee, “Structure-resonant discriminator for image super-resolution,” in *2021 IEEE International Conference on Multimedia and Expo (ICME)* (2021) pp. 1–6.

⁶⁹Y. Xie, Y. Ding, and S. Ji, “Augmented equivariant attention networks for electron microscopy image super-resolution,” CoRR **abs/2011.03633** (2020), 2011.03633.

⁷⁰J. Ling, A. Kurzawski, and J. Templeton, “Reynolds averaged turbulence modelling using deep neural networks with embedded invariance,” Journal of Fluid Mechanics **807**, 155–166 (2016).

⁷¹Y. Yasuda, “equivariant-sr-2d-fluid,” <https://github.com/YukiYasuda2718/equivariant-SR-2D-f1uid> (2022).

⁷²L. Landau and E. Lifshitz, *The Classical Theory of Fields*, fourth edition ed., Course of Theoretical Physics, Vol. 2 (1975).

⁷³X. Du, X. Qu, Y. He, and D. Guo, “Single image super-resolution based on multi-scale competitive convolutional neural network,” Sensors **18** (2018), 10.3390/s18030789.

⁷⁴Y. Zhang, Y. Tian, Y. Kong, B. Zhong, and Y. Fu, “Residual dense network for image super-resolution,” in *Proceedings of the IEEE Conference on Computer Vision and Pattern Recognition (CVPR)* (2018).

⁷⁵R. Keys, “Cubic convolution interpolation for digital image processing,” IEEE Transactions on Acoustics, Speech, and Signal Processing **29**, 1153–1160 (1981).

⁷⁶G. K. Vallis, *Atmospheric and Oceanic Fluid Dynamics: Fundamentals and Large-Scale Circulation*, second edition ed. (Cambridge University Press, 2017).

⁷⁷K. Ishioka, “Ispack 1.0.4,” <https://www.gfd-dennou.org/arch/ispack/index.htm.en> (2015).

⁷⁸K. Taira, A. G. Nair, and S. L. Brunton, “Network structure of two-dimensional decaying isotropic turbulence,” Journal of Fluid Mechanics **795**, R2 (2016).

⁷⁹M. Yoda, “Super-resolution imaging in fluid mechanics using new illumination approaches,” Annual Review of Fluid Mechanics **52**, 369–393 (2020), <https://doi.org/10.1146/annurev-fluid-010719-060059>.

⁸⁰M. Matsuo, T. Nakamura, M. Morimoto, K. Fukami, and K. Fukagata, “Supervised convolutional network for three-dimensional fluid data reconstruction from sectional flow fields with adaptive super-resolution assistance,” (2021), arXiv:2103.09020 [physics.flu-dyn].

⁸¹A. Paszke, S. Gross, F. Massa, A. Lerer, J. Bradbury, G. Chanan, T. Killeen, Z. Lin, N. Gimelshein, L. Antiga, A. Desmaison, A. Kopf, E. Yang, Z. DeVito, M. Raison, A. Tejani, S. Chilamkurthy, B. Steiner, L. Fang, J. Bai, and S. Chintala, “Pytorch: An imperative style, high-performance deep learning library,” in *Advances in Neural Information Processing Systems 32*, edited by H. Wallach, H. Larochelle, A. Beygelzimer, F. d’Alché-Buc, E. Fox, and R. Garnett (Curran Associates, Inc., 2019) pp. 8024–8035.

⁸²T. Cohen, M. Weiler, B. Kicanaoglu, and M. Welling, “Gauge equivariant convolutional networks and the icosahedral CNN,” in *Proceedings of the 36th International Conference on Machine Learning*, Proceedings of Machine Learning Research, Vol. 97, edited by K. Chaudhuri and R. Salakhutdinov (PMLR, 2019) pp. 1321–1330.

⁸³P. D. Haan, M. Weiler, T. Cohen, and M. Welling, “Gauge equivariant mesh {cnn}s: Anisotropic convolutions on geometric graphs,” in *International Conference on Learning Representations* (2021).

⁸⁴A. Campa, T. Dauxois, D. Fanelli, and S. Ruffo, *Physics of Long-Range Interacting Systems* (Oxford University Press, 2014).